Karlsruher Institut für Technologie

Institut für Hochfrequenztechnik und Elektronik

Master Thesis

Investigations on Improving Broadband Boundary Conditions in Gyrotron Interaction Modelling

Chuanren Wu

Supervisor: Dr. Stefan Illy
Dr. Konstantinos A. Avramidis

Period: 05.08. 2013 – 05.02. 2014

Karlsruhe, 29.01. 2014

Postanschrift: Institut für Hochfrequenztechnik und Elektronik
Kaiserstraße 12
D-76131 Karlsruhe

Gebäude: Engesserstraße 5, Geb. 30.10

Tel.: +49 (0) 721 608 4 2522
Sekr.: +49 (0) 721 608 4 2523
Fax: +49 (0) 721 608 4 5027
E-Mail: info@ihe.kit.edu
Web: www.ihe.kit.edu

Declaration

I hereby declare that I wrote my master thesis on my own and that I have followed the regulations relating to good scientific practice of the Karlsruhe Institute of Technology (KIT) in its latest form. I did not use any unacknowledged sources or means and I marked all references I used literally or by content.

Chuanren Wu

Abstract

Gyrotrons are microwave tubes capable of providing mega-watt power at millimetric wavelengths. The microwave power is produced by the conversion of the kinetic energy of an electron beam to electromagnetic wave energy. Simulations of the beam-wave interaction in the gyrotron cavity are essential for gyrotron design, as well as theoretical and experimental studies.

In the usual gyrotron operation the spectrum of the generated radiation is concentrated around the nominal frequency. For this reason, the usual simulations consider only a narrow-band output spectrum (e.g. several GHz bandwidth comparing with the working frequency in the range of 100-200 GHz). As a result, the typical existing codes use a single-frequency radiation boundary condition for the generated electromagnetic field in the cavity. This condition is matched only at one frequency. However, there are two important aspects, which motivate an advanced formulation and implementation of the cavity boundary condition. Firstly, the occurrence of broadband effects (which may be several tens of GHz) in some cases , like dynamic after-cavity-interaction or modulation side-bands, requires a broadband boundary condition. Secondly, there are reflections from inside and outside of the gyrotron, which can only be considered in the simulation through a boundary condition with user-defined, frequency-dependent reflections.

This master thesis proposes an improved formulation of the broadband boundary condition in the self-consistent, beam-wave interaction code EURIDICE. In this new formulation, two physical variables — the wave impedance and the axial wavenumber are expanded in polynomial series in the frequency domain. Because the beam-wave interaction process is simulated transiently in the time domain, the boundary condition should be also expressed in the time domain. This involves a non-trivial inverse Fourier transform, for which two solutions are proposed, tested and validated.

It has been shown that, through the newly developed formulation, the existing matched boundary condition (that should yield zero-reflection in ideal case) can be improved by 15 dB even with a first-order polynomial series. Moreover, a user-defined, frequency-dependent complex reflection coefficient can be introduced. This was not possible with the previously existing boundary condition in EURIDICE.

Contents

1. Introduction **1**

2. Theoretical study of the boundary condition **9**
2.1. Derivation of boundary condition 9
2.1.1. Transmission line theory 9
2.1.2. Boundary condition in frequency domain 10
2.1.3. Approximation of the axial wave number 13
2.1.4. Transforming into the time domain 18
2.2. Solution I: Lebesgue integrable function 18
2.3. Solution II: Distribution 24
2.4. Summary 26

3. Numerical implementation and validation **27**
3.1. Slow time scale 27
3.2. Excitations (source terms) 29
3.3. Numerical methods 31
3.4. Single-frequency matched boundary condition 35
3.5. Broadband boundary condition 36
3.5.1. In the space of tempered distributions 37
3.5.2. In the space of Lebesgue integrable functions 39
3.6. Making use of the polynomial series to advance the state-of-the-art . . 42
3.6.1. Improved wavenumber 44
3.6.2. User defined reflection 44
3.7. Summary 47

4. Summary and outlook **49**

A. Fourier transforms **51**

1. Introduction

Gyrotron description

Gyrotron oscillators are vacuum tubes, which are used to generate megawatt power at millimetre wavelength. They are typically applied as sources for ECRH & CD (Electron Cyclotron Resonance Heating & Current Drive) in fusion experimental reactors, material processing and as gyrotron amplifier in millimetre-wavelength radars [1] [ch. 10]. Fig. 1.1 shows the sketch of a typical gyrotron. The high energy electrons from the electron gun pass through the beam tunnel and travel into the cavity. In the cavity, they will exchange their energy with the electromagnetic RF field (so-called interaction). In this process, a part of the kinetic energy is taken from the electron beam and transformed into the energy of the electromagnetic wave. Afterwards, the electrons are absorbed by the collector, whereas the high power wave is guided through the launcher, steered by a few mirrors and transferred to the outside through a wave-transparent window.

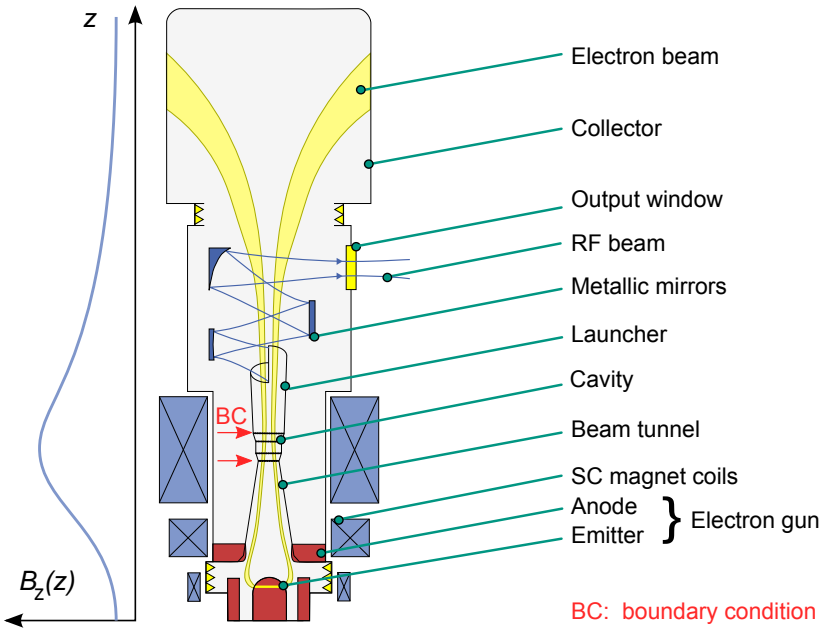

Fig. 1.1.: Sketch of a gyrotron

For some practical reasons, each part of a gyrotron (e.g. the gun, cavity, collector and the quasi-optical system) is simulated separately. In the simulation of cavities, a system consisting of the Maxwell's equations and the motion equation of electrons is solved. The common approach is to solve these two kinds of equations alternatively in a loop as fig. 1.2 shows.

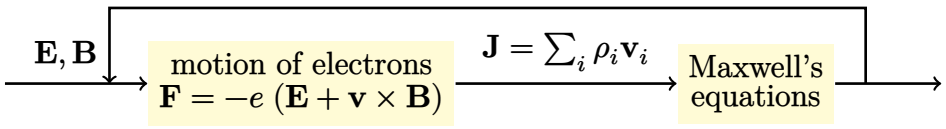

Fig. 1.2.: The common approach to simulate the interaction of the electron beam with the RF wave in the gyrotron cavity

Cavity modelling

A schematic view of the gyrotron cavity is presented in fig. 1.3. It is a part of a waveguide with a mild variation of the radius (typically $< 5°$). The middle section has a constant radius and the radius variation before and after the middle section makes the appearance of standing wave possible. The cavity has open ends, in order for the electromagnetic radiation to be able to leave the region. The geometry is rotationally symmetric around the z-axis. For tolerating high power, the cavity is usually overmoded. The dimension of the cavity as well as the other RF parts is much larger than the wavelength. This means, that it will take a lot of time and resources to simulate the interaction of the electron beam with the electromagnetic field in such overmoded cavity using any well known full-wave analysis. Hence for the purpose of a fast design and parameter studies, the physical model has to be simplified. Firstly, the RF fields

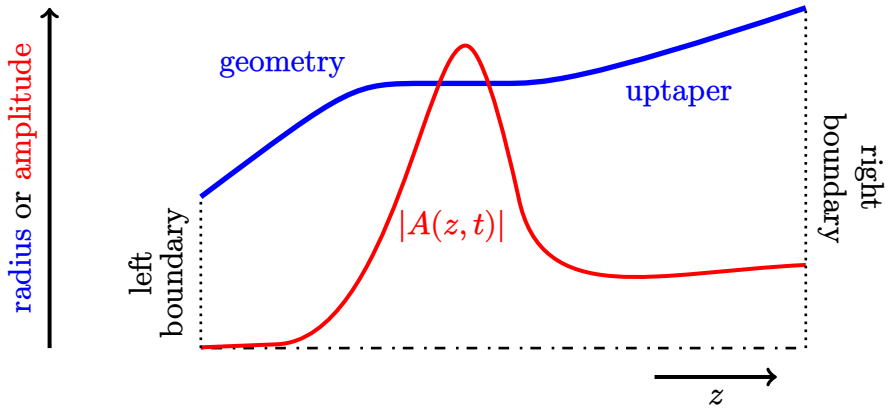

Fig. 1.3.: Schematic sketch of the cavity

are decomposed into transverse eigenmodes. The boundary condition at the open ends of the cavity will be based on this expansion in cylindrical eigenmodes. Secondly, since the transverse structure of the eigenmodes is known, the field representation is reduced to a complex envelope function $A(z,t)$, which is spatially one-dimensional. This function describes the field profile along the gyrotron axis (the z-axis). For a specific TE-mode, the vectorial electric field $\mathbf{E}$ can be written as

$$\mathbf{E}(r,\phi,z,t) = A(z,t)\; e^{j\omega_0 t}\; \mathbf{e}(r,\phi\,;\,z)\;,$$

where ω_0 is a constant carrier frequency. $\mathbf{e}(r,\phi\,;\,z)$ is the mode-specific membrane vector [1] ch. 3. Its parameter z is separated from the other two parameters, because the membrane vector is assumed to vary weakly along the z-axis. Thus, the z-dependence of the field is essentially described by $A(z,t)$.

Boundary condition

The general equation for boundary conditions at the open ends of the cavity in frequency domain is

$$\hat{A}(z,\omega) = \pm\frac{Z}{j\,k_{\parallel}}\frac{\partial\hat{A}(z,\omega)}{\partial z}\;,$$

where $\hat{A}$ is the transformed envelope function A in the frequency domain. Z is a normalized wave-impedance and $k_{\parallel}$ is the axial wavenumber; generally they are both frequency-dependent. The sign on the right-hand side of this equation depends on the side of the boundary. More details will be presented in chapter 2.

An initial assumption for the boundary condition is that the electromagnetic wave can travel through the boundaries of the cavity without being reflected. The commonly used simple boundary condition for a certain mode has zero reflection only at one single frequency, because it treats the Z and $k_{\parallel}$ as constants. This kind of boundary condition can be found in most European simulation codes, such as SELFT [2], EURIDICE [3] , COAXIAL [4] and TWANG [5]. Although this boundary condition has a limited bandwidth, it is still valid in the most cases. This is because the output spectrum of a single mode is as narrow-band as the boundary condition.

However, for several special designs and configurations there are more than one frequency, which appear under a certain mode. An example is the dynamic After-Cavity-Interaction (ACI) effect. The beam-wave interaction is designed to occur merely in the middle section of the cavity, but there is sometimes an undesired energy exchange in the uptaper region. S. KERN et al. observed in [6] that the non-stationary, dynamic

ACI causes the appearance of other frequencies. Furthermore A. SCHLAICH found the spectral lines experimentally, which are suspected to be the dynamic ACI frequencies [7]. Even if the dynamic ACI does not exist physically, through the implementation of a broadband boundary condition the undesired reflection can be excluded from the reasons, which may cause this simulation effect. Another example of multiple frequencies in a single mode is the side-bands described in [8] by S. ALBERTI. For all the above cases, **broadband boundary conditions are required** for a precise simulation.

Broadband matched boundary conditions (i.e. without reflections) already exist in EURIDICE and TWANG. In reality, however there are some reflections at those positions where the structure is not smooth enough, like the launcher, window or even the load outside of the gyrotron. The simulation tools should have the capability to **adopt an arbitrary, frequency-dependent reflection**, for the reason of setting up a more realistic simulation or just for the purpose of observing how an undesired reflection affects the interaction. Most interaction codes can adopt a reflection coefficient for a single frequency. Among them, the code EURIDICE is able to set a constant reflection coefficient for the entire frequency band. However, none of the existing code can handle a user-defined, frequency-dependent reflection yet.

State of the art

The code package EURIDICE has the capability to simulate time-dependent, multi-mode, self-consistent beam-wave interaction and has been successfully used for simulation and design of several gyrotrons in Europe. There is already a broadband matched boundary condition implemented in EURIDICE. Also TWANG is equipped with a matched broadband boundary condition, however it is limited to single-mode calculations. Taking the dynamic ACI in the 140 GHz, 1 MW gyrotron for the stellarator *W7-X* [9] as an example, the current state of the broadband matched boundary condition will be presented here.

Under the $TE_{28,8}$ mode, dynamic ACI can be observed in the simulation of the 140 GHz gyrotron. The radius at the end of the cavity yields for this mode 129.9 GHz cut-off frequency. After the equilibrium state has been reached, the simulation predicts a spectrum shown in fig. 1.4. In the spectrum, one can see the working frequency 140.23 GHz. Except this, a weak dynamic ACI signal is above the noise level, which can be found near the cut-off frequency at 131.3 GHz. The ACI appears, because the energy-exchange criterion (resonance condition) is fulfilled again in the uptaper region. The field profile with the appearance of ACI can be seen in fig. 1.5.

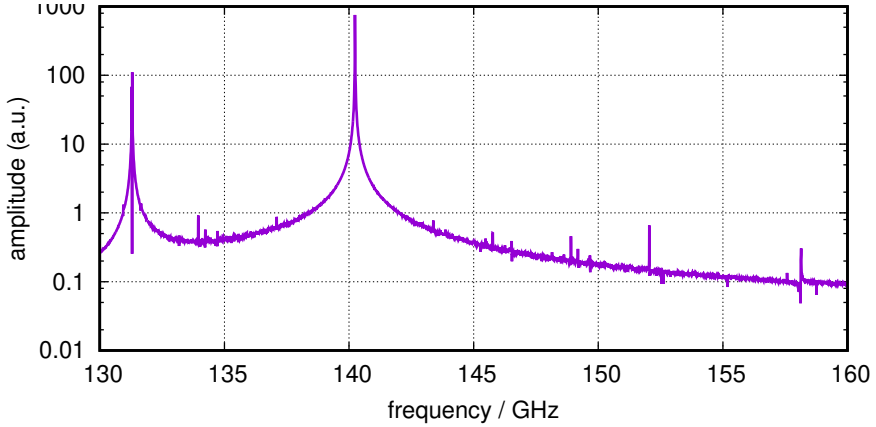

Fig. 1.4.: Spectrum of the 140 GHz gyrotron for *W7-X* with dynamic ACI

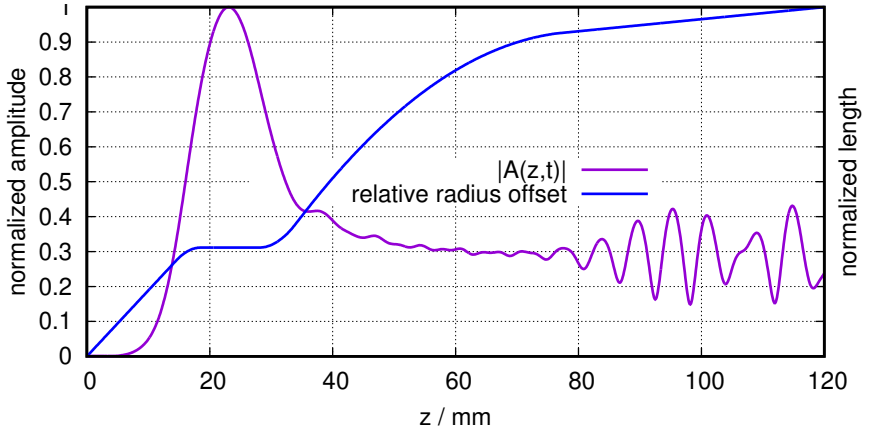

Fig. 1.5.: Field profile for the dynamic ACI case in the 140 GHz gyrotron

The properties of the commonly used single-frequency boundary condition is obtained from the EURIDICE simulation result in fig. 1.6. This boundary condition has a perfect absorption at the carrier frequency (140.20 GHz, which is 30 MHz below the main signal frequency according to fig. 1.4). However, there is considerable[1] reflection at the ACI frequency of 131.3 GHz.

The reflection coefficient of EURIDICE's broadband boundary condition is demonstrated in fig. 1.7 for a time step of 10 ps. It is clear, that this boundary condition absorbs not only the carrier frequency but also the other signals, especially in the frequency band around the dynamic ACI. But the matched band near the ACI in fig. 1.7 is higher than the exact ACI frequency 131.3 GHz. Fig. 1.8 shows the reflection coefficient of the broadband boundary condition with a smaller time discretization

[1] $|\Gamma| \approx 40\%$

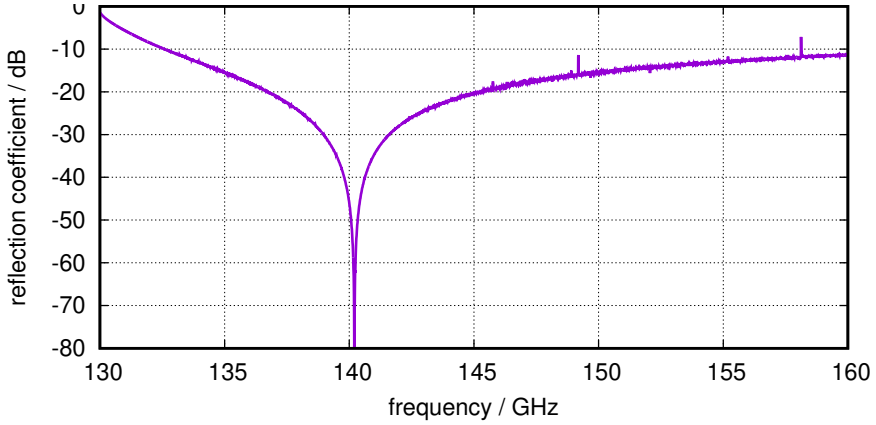

Fig. 1.6.: Reflection of the single frequency boundary condition for *W7-X* ACI simulation in EURIDICE

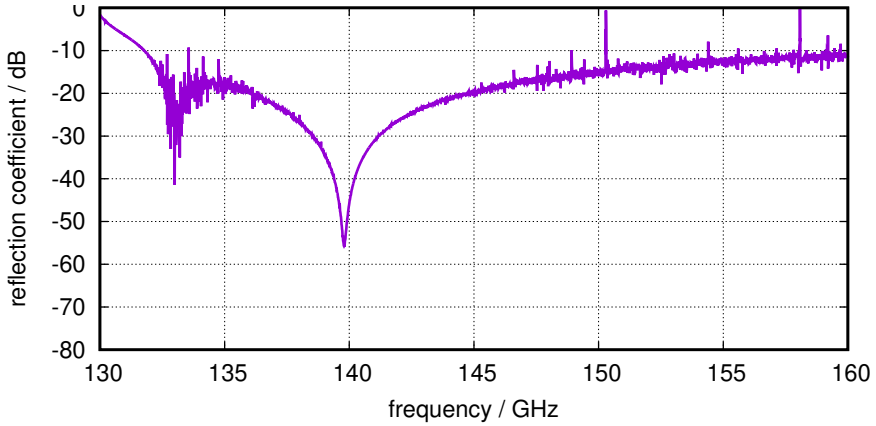

Fig. 1.7.: Reflection of the existing broadband boundary for the spectrum in fig. 1.4 with 10 ps time step

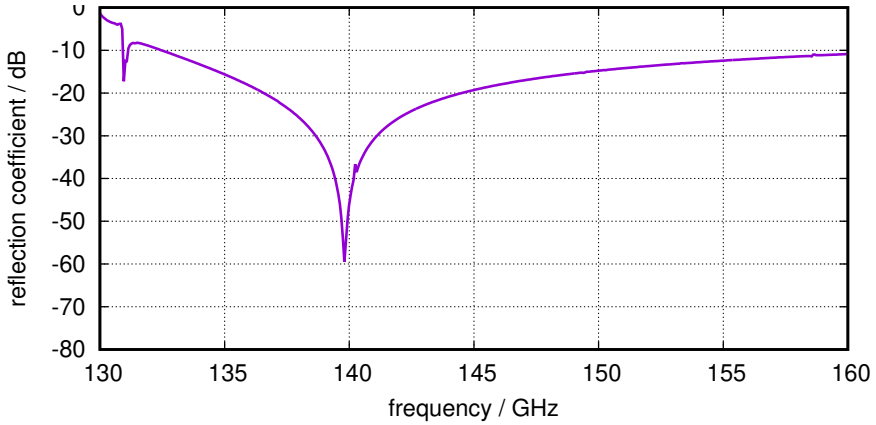

Fig. 1.8.: Reflection of the existing broadband boundary for the spectrum in fig. 1.4 with 1 ps time step

(1 ps). The local optimum moves to the exact dynamic ACI frequency. Besides, the spectrum is much cleaner than the one with a large time discretization.

It can be also observed, that the optimum of the single-frequency boundary condition is a little higher above 140 GHz whereas the optimum of the broadband one is below 140 GHz. The reason is supposed to be the approximation of the wave number (see chapter 2.1.3).

The state of the art, regarding the boundary condition can be summarized as follows:

- The existing matched broadband boundary condition can absorb a multi-frequency spectrum.
- It needs small time discretizations to obtain a clean and reliable result. This leads to very time-consuming simulations.
- At the frequencies where there is no defined signal, the broadband boundary condition handles the correlated noise like the single-frequency boundary condition.
- There is no possibility to set a frequency-dependent reflection.

Goal and outline of this master thesis

This master thesis aims at improving the existing broadband boundary condition, especially at introducing a user-defined, frequency-dependent reflection coefficient to the broadband boundary condition. In chapter 2, the enhanced broadband boundary condition which considers user-defined reflections is derived and two possible solutions to implement this boundary condition are proposed. To verify these two solutions, a numerical program is written during the thesis, which simulates a simple homogeneous dispersive waveguide fed by a user-defined current. The methods and results of the simulations are discussed in chapter 3. Chapter 4 summarizes the ideas as well as results and gives an outlook to the future work. Appendix A gives a short review of the Fourier transforms used in this text.

2. Theoretical study of the boundary condition

2.1. Derivation of boundary condition

2.1.1. Transmission line theory

The electrical values (e.g. the current, voltage or field strength) in a transmission line can be presented generally as the overlap of a forward and a backward propagating wave, shown in the following equation. Γ_f is the reflection coefficient for the forward wave. $E_0 \in \mathbb{C}$ is a constant.

$$E(z) = E_0 \left(e^{j(\omega t - k_\parallel z)} + \Gamma_f e^{j(\omega t + k_\parallel z)} \right) \tag{2.1}$$

Assuming $E(z)$ is differentiable over z

$$\frac{\partial E}{\partial z} = E_0 \left(-jk_\parallel e^{j(\omega t - k_\parallel z)} + jk_\parallel \Gamma_f e^{j(\omega t + k_\parallel z)} \right) \tag{2.2}$$

Multiplying both sides of (2.1) by $jk_\parallel$

$$jk_\parallel E = E_0 \left(jk_\parallel e^{j(\omega t - k_\parallel z)} + jk_\parallel \Gamma_f e^{j(\omega t + k_\parallel z)} \right) \tag{2.3}$$

Summing and subtracting (2.2) and (2.3):

$$\frac{\partial E}{\partial z} + jk_\parallel E = 2jk_\parallel \, \Gamma_f \, E_0 \, e^{j(\omega t + k_\parallel z)} \tag{2.4a}$$

$$\frac{\partial E}{\partial z} - jk_\parallel E = 2jk_\parallel \, \Gamma_f \, E_0 \, e^{j(\omega t - k_\parallel z)} \tag{2.4b}$$

After combining both equations, there is

$$\frac{\partial E}{\partial z} + jk_\parallel E = \left(\frac{\partial E}{\partial z} - jk_\parallel E \right) \Gamma_f e^{j\,2k_\parallel z}$$

The variable z equals to the position, where the corresponding reflection coefficient Γ is given. So if Γ_f is given at $z = 0$, then the relation will be

$$\frac{\partial E}{\partial z} + jk_\parallel E = \left(\frac{\partial E}{\partial z} - jk_\parallel E \right) \Gamma_f \tag{2.5}$$

which can be written as

$$\left(\Gamma_f + 1\right) \frac{\partial E}{\partial z} = \left(\Gamma_f - 1\right) jk_{\|} E \tag{2.6}$$

Doing the same calculation for the backward reflection coefficient Γ_b yields

$$\left(1 + \Gamma_b\right) \frac{\partial E}{\partial z} = \left(1 - \Gamma_b\right) jk_{\|} E \tag{2.7}$$

If both Γ_f and Γ_b do not equal to one, then

$$E = \left(\frac{1+\Gamma}{1-\Gamma}\right) \frac{s}{jk_{\|}} \frac{\partial E}{\partial z} \tag{2.8}$$

where $s = 1$ for the left ($\Gamma = \Gamma_b$) side, $s = -1$ for the right ($\Gamma = \Gamma_f$) side. This is the radiation boundary condition for a field component E at frequency ω in a wave guide.

2.1.2. Boundary condition in frequency domain

Equation (2.8) can be written in a frequency-dependent form explicitly

$$\hat{E}(z_b, \omega) = s \frac{Z(\omega)}{jk_{\|}(\omega)} \left. \frac{\partial \hat{E}(z, \omega)}{\partial z} \right|_{z \to z_b} \tag{2.9}$$

where z_b is the z-coordinate at the boundary. In the following text the condition $z \to z_b$ will be omitted for convenience. $Z(\omega)$ is the normalized wave impedance and it can be expanded in a (truncated) Taylor series around frequency ω_0

$$Z(\omega) = \frac{1+\Gamma(\omega)}{1-\Gamma(\omega)} = \sum_{n=0}^{N_z} a_n \left(\omega - \omega_0\right)^n \tag{2.10}$$

$k_{\|}(\omega)$ is the axial wave number, for a dispersive waveguide, it equals

$$k_{\|}(\omega) = \frac{1}{c_0} \sqrt{\omega^2 - \omega_c^2}^{\dagger} \tag{2.11}$$

where

- c_0 is the velocity of the light in the medium.
- ω_c is the cut-off frequency of a certain mode.
- $\sqrt{x}$ indicates the square root with a non-negative real part i.e.

$$-\frac{\pi}{2} \leq \arg\left\{\sqrt{z}\right\} \leq \frac{\pi}{2}$$

- $x^\dagger$ stands for the complex conjugate of x.

The axial wavenumber $k_\parallel$ should be the conjugate of the square root with a non-negative real part. According to the field modelling in (2.1), the wavenumber should be positive above the cut-off frequency, so that the wave $e^{j(\omega t \pm k_\parallel z)}$ propagates in the defined direction. When below cut-off, its imaginary part has to be negative, in order to attenuate the wave while it is travelling outside from the cavity. The wavenumber $k_\parallel$ will be discussed again in chapter 2.1.3.

The time-dependent TE-mode RF field in the cavity is modelled as a narrow-band amplitude modulation on the carrier frequency ω_0.

$$\mathbf{E}(r, \phi, z, t) = A(z, t) e^{j\omega_0 t}\, \mathbf{e}(r, \phi; z) \tag{2.12}$$

$\omega_0 \in \mathbb{R}$ is the carrier frequency, usually chosen as the resonance frequency of the cold cavity (the cavity without the electron beam). $A(z, t)$ is the complex amplitude profile of the field. $\mathbf{e}(r, \phi; z)$ is the membrane vector in the cylindrical coordinate [1]ch. 3, which is assumed to vary slowly along the z axis (i.e. $\left|\frac{\partial \mathbf{e}}{\partial z}\right| \frac{1}{|\mathbf{e}|} \ll \left|\frac{\partial A}{\partial z} \frac{1}{A}\right|$) and there is

$$\left(\nabla_\perp^2 + k_\perp^2\right)\ \mathbf{e}(r, \phi; z) = 0 \tag{2.13}$$

where

$$k_\perp^2 = \mu\epsilon\,\omega^2 - k_\parallel^2$$
$$\nabla_\perp^2 = \nabla^2 - \frac{\partial^2}{\partial z^2}$$

The Fourier transform[1] of (2.12) yields

$$\hat{\mathbf{E}}(r, \phi, z, \omega) = \sqrt{2\pi}\ \hat{A}(z, \omega) * \delta(\omega - \omega_0)\ \mathbf{e}(r, \phi; z) \tag{2.14}$$

The asterisk denotes a convolution. According to lemma 1 from appendix A

$$\hat{\mathbf{E}}(r, \phi, z, \omega) = \sqrt{2\pi}\ \hat{A}(z, \omega - \omega_0)\ \mathbf{e}(r, \phi; z) \tag{2.15}$$

with the definition of the envelope's frequency ω_a

$$\omega_a := \omega - \omega_0 \tag{2.16}$$

the field expression becomes

$$\hat{\mathbf{E}}(r, \phi, z, \omega) = \sqrt{2\pi}\ \hat{A}(z, \omega_a)\ \mathbf{e}(r, \phi; z) \tag{2.17}$$

Therefore

$$\frac{\partial \hat{\mathbf{E}}}{\partial z} = \sqrt{2\pi}\ \frac{\partial \hat{A}(z, \omega_a)}{\partial z}\ \mathbf{e}(r, \phi; z) + \sqrt{2\pi}\ \hat{A}(z, \omega_a) \underbrace{\frac{\partial \mathbf{e}(r, \phi; z)}{\partial z}}_{\approx 0} \tag{2.18}$$

[1] see the definition in appendix A

Substituting (2.18) into (2.9) and eliminating $\mathbf{e}(r, \phi, z)$ on both sides

$$\left[\hat{A}(z, \omega_a) = s \frac{Z(\omega)}{j\, k_{\parallel}(\omega)} \frac{\partial \hat{A}(z, \omega_a)}{\partial z} \right]_{z \text{ at boundaries}} \tag{2.19}$$

with $s = 1$ for the boundary on the left-hand (gun) side, -1 for the right-hand (launcher) side. This is the boundary condition for the field envelope function in frequency domain.

Since the envelope function is simulated in the time domain, there is the need to have a formulation of the boundary condition also in the time domain. Two kinds of approaches can be found in the existing simulation codes like EURIDICE:

1. Assuming Z and $k_{\parallel}$ to be frequency independent, e.g. fixing the values of $Z(\omega)$ and $k(\omega)$ at $Z(\omega_0)$ and $k(\omega_0)$, respectively. $\hat{A}(z, \omega_a)$ is inverse Fourier transformed into $A(z, t)$. Then this is the **single-frequency boundary condition**

$$A(z, t) = s \frac{Z(\omega_0)}{j\, k_{\parallel}(\omega_0)} \frac{\partial A(z, t)}{\partial z} \tag{2.20}$$

2. Still keeping Z frequency-independent, but allowing $k_{\parallel}(\omega)$ varying with the frequency, the broadband boundary condition comes out by transforming (2.19) in the time domain[2]:

$$A(z, t) = s\, \frac{Z(\omega_0)}{j\sqrt{2\pi}} \left(\mathcal{F}^{-1} \frac{1}{k_{\parallel}(\omega)} \right) * \frac{\partial A(z, t)}{\partial z} \tag{2.21}$$

   However, the current existing broadband boundary condition does not allow Z also be frequency-dependent.

When taking the second approach, the exact form (2.11) for $\frac{1}{k_{\parallel}(\omega)}$ can be easily inverse Fourier transformed neither analytically nor digitally. The discrete Fourier transform does not work in the common sense, since the wavenumber is in the denominator, which causes numerical infinity at the cut-off frequency. Approximated forms of $k_{\parallel}$ which are more suitable for the analytical Fourier transform, will be discussed in the next section.

[2] see lemma 2 in appendix A

2.1.3. Approximation of the axial wave number

In order to make the analytical inverse Fourier transform in (2.21) easier, the function $k_\parallel(\omega)$ should be simplified. There are at least three ways to approximate the wavenumber. These three methods will be explained and compared in this section and an improvement will be proposed. With the definition

$$\Delta\omega := \omega_0 - \omega_c \tag{2.22}$$

it is assumed in this thesis, that

- $A(z, \omega_a) \approx 0$ for $|\omega_a| \gg 0$
- ω_c and ω_0 are so near, that $\Delta\omega \ll \omega_c, \omega_0$

The first point is the basic assumption for the approximations of $k_\parallel(\omega)$. The second assumption can be weaker, when the compensation discussed at the end of this section is used.

The first kind of approximation

Function $k_1 : \mathbb{R} \to \mathbb{C}$ defines the first approximation of the axial wavenumber.

$$k_1(\underbrace{\omega_a + \omega_0}_{=\omega}) = \begin{cases} \frac{1}{c_0}\sqrt{|(\omega_a+\omega_0)^2 - (\omega_0 - \Delta\omega)^2|} & \text{for } |\omega_a + \omega_0| \geq \omega_c \\ -j\frac{1}{c_0}\sqrt{|(\omega_a+\omega_0)^2 - (\omega_0 - \Delta\omega)^2|} & \text{for } |\omega_a + \omega_0| < \omega_c \end{cases}$$

$$= \begin{cases} \frac{1}{c_0}\sqrt{\left|\cancel{\omega_a^2} + 2(\omega_a + \Delta\omega)\omega_0 - \cancel{\Delta\omega^2}\right|} & \text{for } \begin{array}{l} \omega_a + \Delta\omega \geq 0 \\ \cancel{\omega_a + \Delta\omega \leq -2\omega_c} \end{array} \\ -j\frac{1}{c_0}\sqrt{\left|\cancel{\omega_a^2} + 2(\omega_a + \Delta\omega)\omega_0 - \cancel{\Delta\omega^2}\right|} & \text{for } \cancel{-2\omega_c <} \omega_a + \Delta\omega < 0 \end{cases}$$

Some terms are cancelled because they are either negligible or out of the frequency range of interest. Finally, the approximated wavenumber becomes

$$k_1(\omega_a + \omega_0) = \begin{cases} \frac{\sqrt{2\omega_0}}{c_0}\sqrt{\omega_a + \Delta\omega} & \text{for } \omega_a + \Delta\omega \geq 0 \\ -j\frac{\sqrt{2\omega_0}}{c_0}\sqrt{-(\omega_a + \Delta\omega)} & \text{for } \omega_a + \Delta\omega < 0 \end{cases} \tag{2.23}$$

The second kind of approximation

Another approximation is used in [10], with the leading coefficient $\sqrt{\omega_0}$ replaced by $\sqrt{\omega_c}$. It can be derived in the similar way. Since $(\omega_a + \Delta\omega)^2$ is negligible in the frequency range of interest:

$$\begin{aligned}\sqrt{(\omega_a+\omega_0)^2-\omega_c^2}^{\dagger} &= \sqrt{(\omega_a+\Delta\omega+\omega_c)^2-\omega_c^2}^{\dagger} \\ &= \sqrt{\cancel{(\omega_a+\Delta\omega)^2}+2(\omega_a+\Delta\omega)\omega_c}^{\dagger} \\ &= \sqrt{2\omega_c}\sqrt{\omega_a+\Delta\omega}^{\dagger}\end{aligned}$$

The entire k can be written as

$$k_2(\omega_a+\omega_0) = \begin{cases} \dfrac{\sqrt{2\omega_c}}{c_0}\sqrt{\omega_a+\Delta\omega} & \text{for } \omega_a+\Delta\omega \geq 0 \\ -j\dfrac{\sqrt{2\omega_c}}{c_0}\sqrt{-(\omega_a+\Delta\omega)} & \text{for } \omega_a+\Delta\omega < 0 \end{cases} \tag{2.24}$$

Like the first one, this approximation also obtains the exact value at the cut-off frequency. But the wave number at the carrier frequency has a little deviation, i.e.

$$\begin{aligned} k_2(\omega_c) &= k_{\text{exact}}(\omega_c) = 0 \\ k_2(\omega_0) &\neq k_{\text{exact}}(\omega_0) \end{aligned}$$

This is implemented in EURIDICE.

The third kind of approximation

The third approximation is an average of the first two. Again considering the term under the square root:

$$\begin{aligned}\sqrt{(\omega_a+\omega_0)^2-\omega_c^2}^{\dagger} &= \sqrt{(\cancel{\omega_a}+\omega_0+\omega_c)(\omega_a+\omega_0-\omega_c)}^{\dagger} \\ &= \sqrt{\omega_0+\omega_c}\sqrt{\omega_a+\Delta\omega}^{\dagger}\end{aligned}$$

The term ω_a is cancelled, because its range of interest is assumed to be much smaller than the value of ω_c and ω_0.

$$k_3(\omega_a+\omega_0) = \begin{cases} \dfrac{\sqrt{\omega_0+\omega_c}}{c_0}\sqrt{\omega_a+\Delta\omega} & \text{for } \omega_a+\Delta\omega \geq 0 \\ -j\dfrac{\sqrt{\omega_0+\omega_c}}{c_0}\sqrt{-(\omega_a+\Delta\omega)} & \text{for } \omega_a+\Delta\omega < 0 \end{cases} \tag{2.25}$$

and it always holds

$$k_3(\omega_0) = k_{\text{exact}}(\omega_0)$$
$$k_3(\omega_c) = k_{\text{exact}}(\omega_c)$$

Comparison of the first three approximations

In this section the boundary setting of the 140 GHz gyrotron is used as an example. The cavity of this gyrotron has $\approx 129.9\,\text{GHz}$ cut-off frequency on the right-hand (launcher) side. ω_0 is chosen at 140 GHz. The three above mentioned approximations of $k_\parallel$ will be compared. Fig. 2.1 and 2.2 are the absolute and relative errors of each approximation. From both figures it can be seen, that k_3 is a good compromise. Besides, k_3 equals to the exact $k_\parallel$ at the carrier frequency. But the relative error at cut-off is not zero. The reason for that will be clarified in the next paragraph.

Improved approximation of the axial wave number

It is possible to let the approximation (2.25) converge to the exact value, since

1. $k_\parallel$ in (2.11) is zero if and only if $\omega = \omega_c$. When this happens, k_3 equals to the exact wave number.
2. Otherwise, the error between k_3 and the exact $k_\parallel$ can be expanded in an Taylor series at the point $\omega_a \to 0$. By using this series, the modified k_3 will converge to the exact $k_\parallel$.

This section focuses on the details of the second point. Dividing (2.25) by (2.11) yields

$$\left.\frac{k_3}{k_{\text{exact}}}\right|_{k\neq 0} = \begin{cases} \sqrt{\dfrac{\omega_0+\omega_c}{\omega_a+\omega_0+\omega_c}} & \text{for } \omega_a > -(\omega_0+\omega_c) \\ -j\sqrt{-\dfrac{\omega_0+\omega_c}{\omega_a+\omega_0+\omega_c}} & \text{for } \omega_a < -(\omega_0+\omega_c) \end{cases} \tag{2.26}$$

The branch $\omega_a < -(\omega_0+\omega_c)$ means that the modulated envelope has much broader frequency spectrum than the carrier, which breaks down the essential assumptions of the slow time variation[3]. So this case will not be taken into account. Then (2.26) will be written as

$$\left.\frac{k_3}{k_{\text{exact}}}\right|_{k\neq 0} = \sqrt{\frac{\omega_0+\omega_c}{\omega_a+\omega_0+\omega_c}} \tag{2.27}$$

[3]This is discussed further in chapter 3.1.

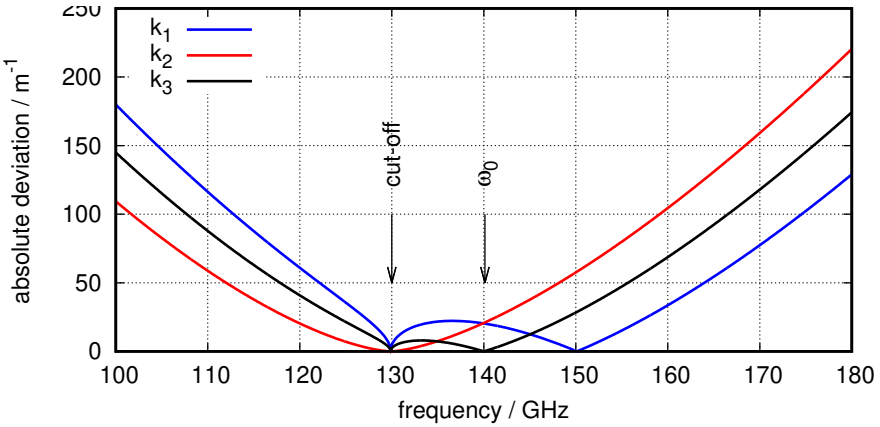

Fig. 2.1.: Absolute deviation of the approximated wave numbers $|k_n - k_{\text{exact}}|$

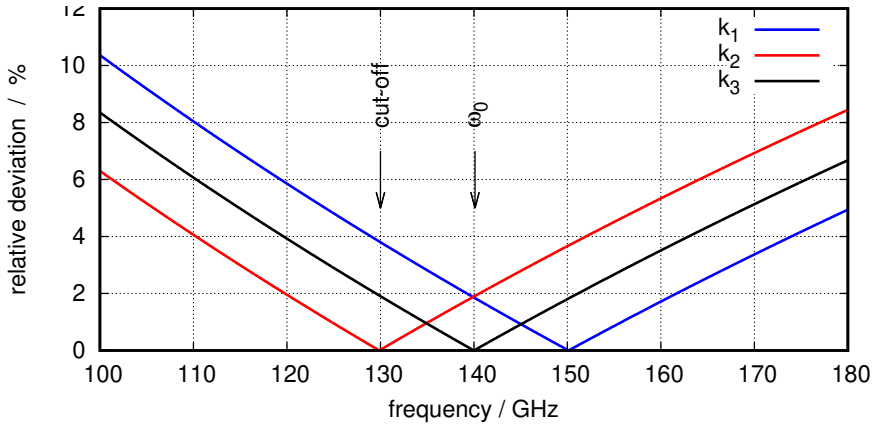

Fig. 2.2.: Relative deviation of the approximated wave numbers $\left|\frac{k_n - k_{\text{exact}}}{k_{\text{exact}}}\right|$

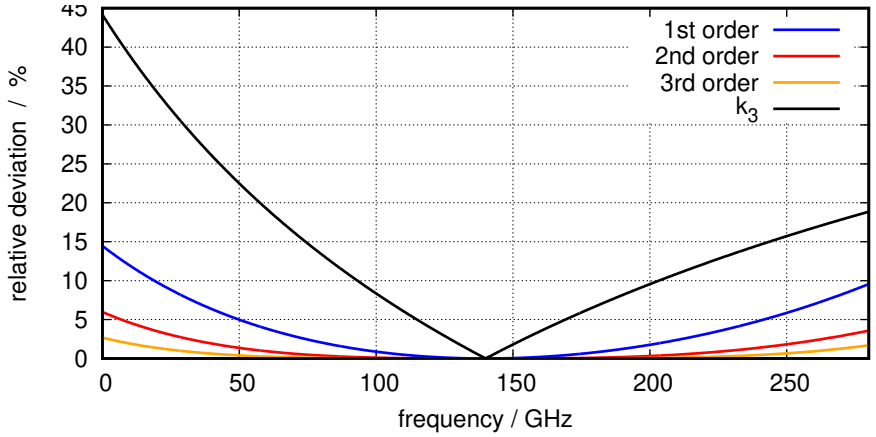

Fig. 2.3.: Relative deviation of the improved axial wave number with different order polynomials

In order to study the behaviour of the ratio at cut-off frequency, ω_a will be substituted with

$$\omega_a = \underbrace{\varepsilon + \omega_c}_{=\omega} - \omega_0$$

$\varepsilon \in \mathbb{R}$ is a small value near zero.

$$\frac{k_3}{k_{\text{exact}}} = \sqrt{\frac{(\omega_0 + \omega_c)\varepsilon}{(\varepsilon + \omega_c)^2 - \omega_c^2}}$$

Applying de L'Hôpital's rule results in

$$\left.\frac{k_3}{k_{\text{exact}}}\right|_{k_{\text{exact}} \to 0} = \left.\sqrt{\frac{(\omega_0 + \omega_c)\varepsilon}{(\varepsilon + \omega_c)^2 - \omega_c^2}}\right|_{\varepsilon \to 0} = \sqrt{\frac{\omega_0 + \omega_c}{2\omega_c}} \tag{2.28}$$

For $\omega_c = 130\,\text{GHz}$ and $\omega_0 = 140\,\text{GHz}$, this value equals to 1.019. This explains, why the relative error at cut-off in fig. 2.2 does not equal to zero ($101.9\% - 100\% = 1.9\%$ at $130\,\text{GHz}$).

Now this error ratio will be used for improving the approximation, by expanding (2.27) into Taylor series

$$\left.\frac{1}{k_{\text{exact}}}\right|_{k \neq 0} = \frac{1}{k_3} \left\{ \sum_{n=0}^{\infty} \frac{1 \cdot 3 \cdot 5 \cdots (2n-1)}{2^n\, n!} \frac{(-1)^n}{(\omega_0 + \omega_c)^n}\, \omega_a^n \right\} \tag{2.29}$$

Its first three terms are

$$\left.\frac{1}{k_{\text{exact}}}\right|_{k \neq 0} \approx \frac{1}{k_3} \left\{ 1 - \frac{1}{2}\left(\frac{\omega_a}{\omega_0 + \omega_c}\right) + \frac{3}{8}\left(\frac{\omega_a}{\omega_0 + \omega_c}\right)^2 - \frac{5}{16}\left(\frac{\omega_a}{\omega_0 + \omega_c}\right)^3 \right\} \tag{2.30}$$

Their relative errors are presented in fig. 2.3. It can be seen that even the first order polynomial improves the accuracy significantly. In addition, this polynomial can be merged into (2.10) in the final calculation.

Conclusion

The final choice of wave number is the approximation based on k_3 and improved through a polynomial series. For practical reasons, this polynomial is truncated until the N_k-th order. Even a truncation at the first order will bring significant advances. Since the inverse of k is used in (2.19), the polynomial refers to $\frac{1}{k}$ instead k itself.

$$\frac{1}{k(\omega_a)} \approx \frac{c_0}{\sqrt{\omega_0 + \omega_c}\,\sqrt{\omega_a + \Delta\omega}^{\,\dagger}} \sum_{n=0}^{N_k} \frac{1 \cdot 3 \cdot 5 \cdots (2n-1)}{2^n\, n!} \frac{(-1)^n}{(\omega_0 + \omega_c)^n}\, \omega_a^n \tag{2.31}$$

2.1.4. Transforming into the time domain

Setting (2.10) and (2.31) into (2.19) and merging the two polynomials together results in

$$\hat{A}(z,\omega_a) = \frac{c_0}{\sqrt{\omega_0+\omega_c}} \left\{ \frac{1}{j\sqrt{\omega_a+\Delta\omega}^{\dagger}} \sum_{n=0}^{N_z+N_k} a_n \left(\omega_a+\Delta\omega\right)^n \right\} \frac{\partial \hat{A}(z,\omega_a)}{\partial z} \tag{2.32}$$

Through lemma 1 from appendix A, the expression in the parenthesis can be shifted by $\Delta\omega$

$$\hat{A}(z,\omega_a) = \frac{c_0}{\sqrt{\omega_0+\omega_c}} \left\{ \delta(\omega_a+\Delta\omega) \ * \sum_{n=0}^{N_z+N_k} a_n \frac{\omega_a^n}{j\sqrt{\omega_a}^{\dagger}} \right\} \frac{\partial \hat{A}(z,\omega_a)}{\partial z} \tag{2.33}$$

Now this equation will be inverse Fourier transformed into the time domain. Lemma 2 is used to map the product into a convolution

$$A(z,t) = \frac{c_0}{\sqrt{\omega_0+\omega_c}} \left\{ \frac{1}{\sqrt{2\pi}} \mathcal{F}^{-1} \left(\delta(\omega_a+\Delta\omega) * \sum_{n=0}^{N_z+N_k} a_n \frac{\omega_a^n}{j\sqrt{\omega_a}^{\dagger}} \right) \right\} * \frac{\partial A(z,t)}{\partial z} \tag{2.34}$$

using lemma 2 yet again from convolution to multiplication and doing an inverse Fourier on the δ-function according to lemma 3

$$A(z,t) = \frac{1}{\sqrt{2\pi}} \frac{c_0}{\sqrt{\omega_0+\omega_c}} \left\{ e^{-j\Delta\omega t} \mathcal{F}^{-1} \sum_{n=0}^{N_z+N_k} a_n \frac{\omega_a^n}{j\sqrt{\omega_a}^{\dagger}} \right\} * \frac{\partial A(z,t)}{\partial z} \tag{2.35}$$

After sorting the components, the following expression for the broadband boundary condition in time domain arises

$$A(z,t) = \frac{1}{\sqrt{2\pi}} \frac{c_0}{\sqrt{\omega_0+\omega_c}} \sum_{n=0}^{N_z+N_k} a_n \left(\left\{ e^{-j\Delta\omega t} \mathcal{F}^{-1} \frac{\omega_a^n}{j\sqrt{\omega_a}^{\dagger}} \right\} * \frac{\partial A(z,t)}{\partial z} \right) \tag{2.36}$$

Two solutions for calculating the right-hand side of this equation are discussed in the following.

2.2. Solution I: Lebesgue integrable function

The (improper) integral $\int_0^x \frac{\omega^n}{\sqrt{\omega}^{\dagger}} \, \mathrm{d}\omega$, $n \in \mathbb{N}$, exists for $x < \infty$. This means, if the value of the integrand can be limited at $x \to \infty$, then the Fourier transform in (2.36) is able to be performed in $\mathcal{L}^1$ space. Because of the slow-time-scale assumption, the spectrum of the envelope function on the left-hand side of (2.33) is concentrated around

$\omega \approx 0$. So the value of $\omega^{n-0.5}$ is less important at $\omega \to \pm\infty$ than its value at $\omega \approx 0$. Therefore a low-pass filter $h(\omega)$ will be designed to suppress the integrand's value at high frequencies. Thus (2.36) can be reformed as

$$A(z,t) = \frac{c_0}{\sqrt{\omega_0 + \omega_c}} \frac{1}{\sqrt{2\pi}} \left(e^{-j\,\Delta\omega\, t}\ \mathcal{F}^{-1} g \right) * \frac{\partial A(z,t)}{\partial z} \tag{2.37}$$

where

$$g(\omega) = \left(\sum_{n=0}^{N_z+N_k} a_n \frac{\omega^n}{j\sqrt{\omega}^{\dagger}} \right)\ h(\omega) \tag{2.38}$$

There are a few conventional low-pass filters, like the Butterworth-filter, which may limit the amplitude of that polynomial function at high frequencies. However, such filters have two disadvantages. Firstly, they are polynomial filters. For a strong decaying ramp, the order of these filters has always to be much higher than the function order $N_z + N_k$. This may cause numerical overflows and inaccuracies when summing and evaluating the polynomials. Secondly, these filters have linear phase, which will also influence the phase of $A(z,\omega)$ in a broadband spectrum.

Another kind of filter which may overcome the disadvantages of those polynomial filters is the Gaussian filter, see fig. 2.4. It has the form

$$h(\omega) = e^{-\left(\frac{\omega}{\Omega}\right)^2} \tag{2.39}$$

However, the Fourier transform $\mathcal{F}^{-1}\left\{ \frac{\omega^n}{\sqrt{\omega}^{\dagger}}\ e^{-\omega^2} \right\}$ yields terms like $t^n\ e^{-\frac{t^2}{8}} \mathcal{I}_{\frac{5}{4}}\left(\frac{t^2}{8}\right)$, where $\mathcal{I}$ is the modified Bessel function. Such terms are hard to be evaluated numerically, since there is a zero multiply infinity problem for a large t.

The final idea is a filter, starting from an even function, which has on both sides the same exponential decays

$$h_e(\omega) = e^{-\left|\frac{\omega}{\Omega}\right|} \tag{2.40}$$

where $\Omega \in \mathbb{R}^+$ is the initial bandwidth. A sketch of this function is shown in fig. 2.5. Although the symmetric exponential function limits the polynomial-like spectrum into $\mathcal{L}^1$ space, it does not have a flat amplitude at the desired passing band. This can be solved by compensating the filter function with a truncated polynomial, which comes from the Taylor series of its complementary function $\frac{1}{h_e(\omega)} = e^{+\left|\frac{\omega}{\Omega}\right|}$

$$\tilde{h}_e(\omega) = \sum_{n=0}^{N_h} \frac{1}{n!} \left(\frac{1}{\Omega}\right)^n |\omega|^n$$

In case of $N_h \to \infty$, the product of $h_e(\omega)$ and $\tilde{h}_e(\omega)$ converges to unity. Hence the final filter function consists of these two parts

$$h(\omega) = h_e(\omega) \cdot \tilde{h}_e(\omega) = \left(\sum_{n=0}^{N_h} \frac{1}{n!} \left(\frac{1}{\Omega}\right)^n |\omega|^n \right) e^{-|\frac{\omega}{\Omega}|} \tag{2.41}$$

Fig. 2.6 presents the filter function for different N_h, drawn in normalized units.

The function to be Fourier transformed, which is the $g(\omega)$ in (2.38), will now be

$$\begin{aligned} g(\omega) &= \begin{cases} -j \left(\sum_{n=0}^{N_h} \frac{1}{n!} \left(\frac{1}{\Omega}\right)^n \omega^n \right) \left(\sum_{n=0}^{N_z+N_k} a_n \omega^n \right) e^{-\frac{\omega}{\Omega}} \frac{1}{\sqrt{\omega}} & \text{for } \omega > 0 \\ \left(\sum_{n=0}^{N_h} \frac{1}{n!} \left(\frac{1}{\Omega}\right)^n (-1)^n \omega^n \right) \left(\sum_{n=0}^{N_z+N_k} a_n \omega^n \right) e^{+\frac{\omega}{\Omega}} \frac{1}{\sqrt{-\omega}} & \text{for } \omega < 0 \end{cases} \\ &= \begin{cases} \sum_{n=0}^{N} \alpha_n \omega^n e^{-\frac{\omega}{\Omega}} \frac{1}{\sqrt{\omega}} & \text{for } \omega > 0 \\ \sum_{n=0}^{N} \beta_n \omega^n e^{\frac{\omega}{\Omega}} \frac{1}{\sqrt{-\omega}} & \text{for } \omega < 0 \end{cases} \end{aligned} \tag{2.42}$$

In (2.42) α_n and β_n are complex coefficients, N is the sum of N_z, N_k and N_h. It can be proven easily that $g(\omega)$ belongs to $\mathcal{L}^1(\mathbb{R})$. Thus its Fourier transform is defined as (A.2). The integral over the whole frequency axis can be separated into two intervals — the positive ω and negative ω, both integrals are analytically solvable through

$$\frac{1}{\sqrt{2\pi}} \int_0^\infty \frac{\omega^n}{\sqrt{\omega}} e^{-\frac{\omega}{\Omega}} e^{j\omega t} \, \mathrm{d}\omega = \frac{1}{\sqrt{2}} \frac{\prod_{p=1}^{n}(2p-1)}{2^n} \left(\frac{1}{\Omega} - jt\right)^{-\frac{2n+1}{2}} \tag{2.43a}$$

$$\frac{1}{\sqrt{2\pi}} \int_{-\infty}^0 \frac{\omega^n}{\sqrt{-\omega}} e^{\frac{\omega}{\Omega}} e^{j\omega t} \, \mathrm{d}\omega = \frac{1}{\sqrt{2}} (-1)^n \frac{\prod_{p=1}^{n}(2p-1)}{2^n} \left(\frac{1}{\Omega} + jt\right)^{-\frac{2n+1}{2}} \tag{2.43b}$$

An advantage of this solution is the limited signal bandwidth, through which the required time discretization can be estimated. The requirement of time discretization for the filter (which may dominate the global time discretization) is decided by the aliasing effect. As shown in fig. 2.7, when refering to the filter, the term “bandwidth” is defined through an amplitude drop by 0.1 and maximal $-20\,\mathrm{dB}$ aliasing is allowed by default. Under this condition, the time discretization has to be smaller than $\frac{1}{b_2}$ (see the figure). The value of b_2 and Ω are simply calculated by a binary search algorithm. Table 2.1 is a comparison of the influence of order and bandwidth to the time discretization. It shows:

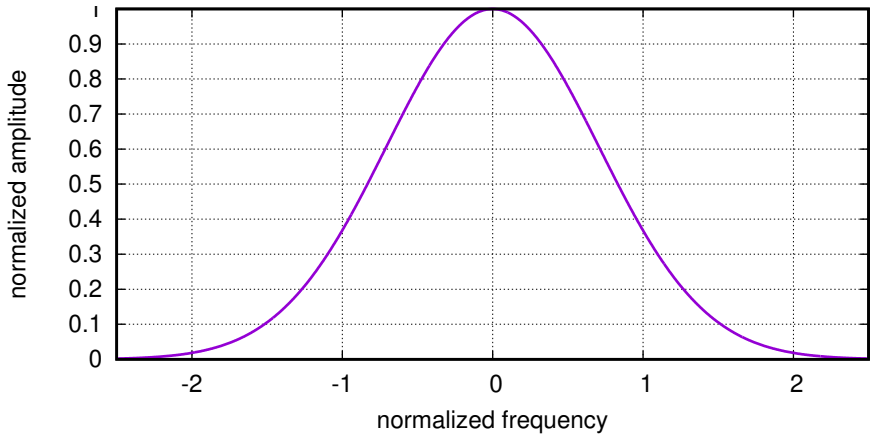

Fig. 2.4.: Spectrum of a normalized Gaussian filter

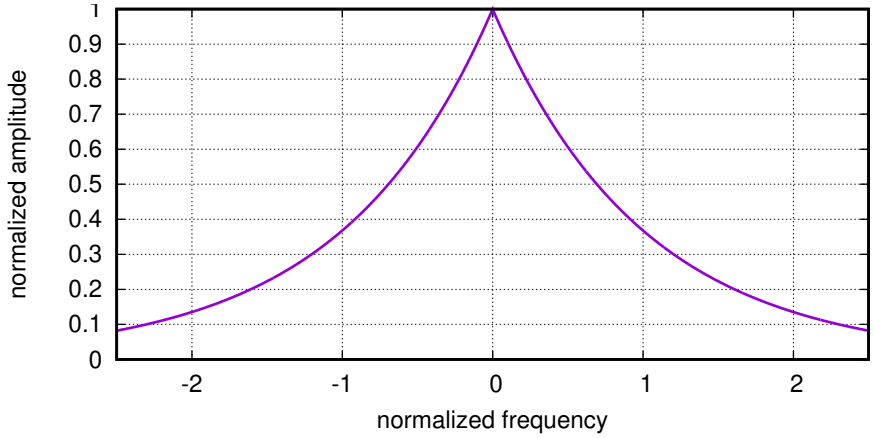

Fig. 2.5.: Spectrum of a normalized exponential filter

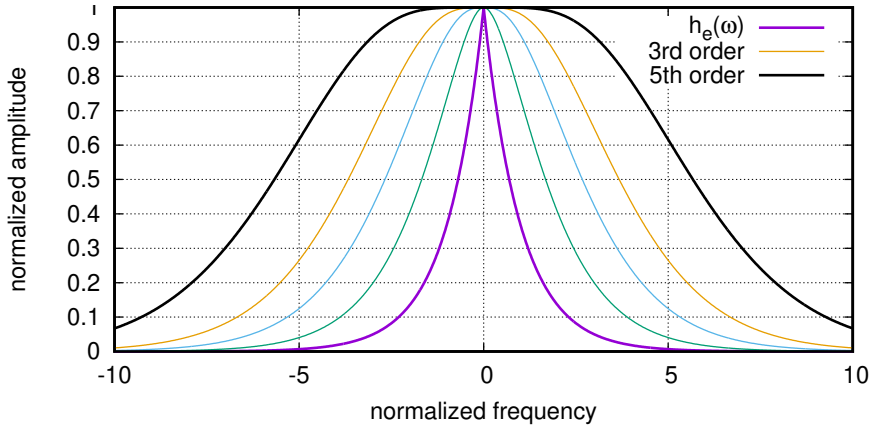

Fig. 2.6.: The filter function $h(\omega)$ with different orders of polynomial compensation

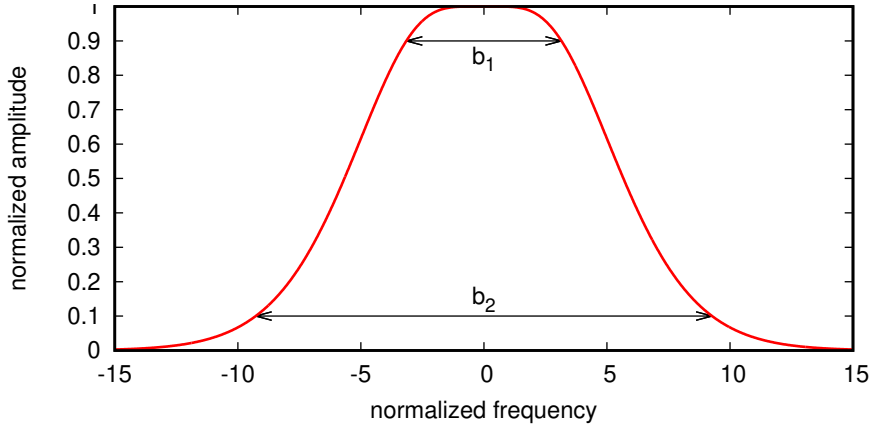

Fig. 2.7.: Bandwidth and the aliasing threshold of the exponential filter

Table 2.1.: Comparison of different filter parameters

order	double side bandwidth in GHz	Ω in GHz	max. time discretization in ns
0	20	596.35	0.002
3	20	36.01	0.013
3	40	72.02	0.007
7	20	13.49	0.020
7	40	26.99	0.010
9	20	10.10	0.022
15	20	5.64	0.026
30	20	2.61	0.031

- Doubling the frequency band will halve the time discretization.
- The relation between the order of the filter and its required time discretization is not linear. The maximal allowed time discretization will be saturated during the increasing of the number of the filter's order and a high-order filter is inconvenient for the numerical evaluation. Thus it seems that the optimal order should be around 10.

Causality

With the consequence of the last paragraph, (2.37) as well as (2.36) are well defined. But the filter in (2.41) has an unwanted property, namely the *non-causality*. This

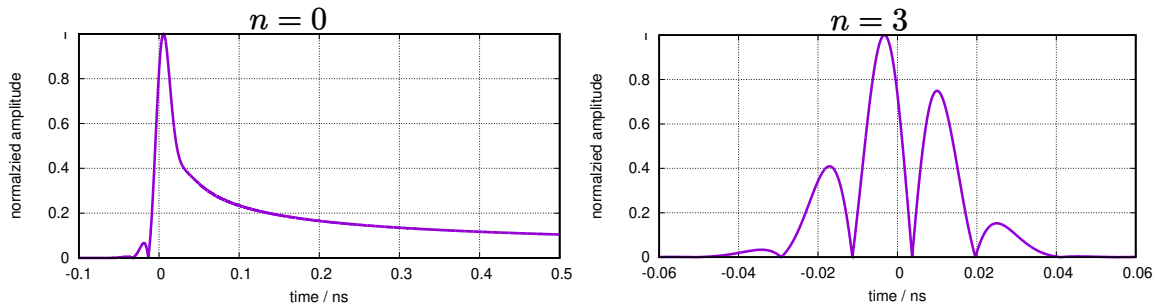

Fig. 2.8.: Time signal $\psi_n(t)$ with different order n

belongs to the features of the so called "zero-phase-filters". Since the primary task of usual simulation codes is predicting the consequence under a given condition, the data in the far future are therefore not available before they've been calculated. It should be avoided, that any data from the far future appears in the formulation of boundary conditions. Three approaches have been investigated, through which, the effects of the non-causality may be circumvented:

1. omitting the whole non-causal part
2. delaying the filter linearly and compensating the dispersion (i.e. phase-errors) caused by the time-delay, again through a polynomial
3. delaying the filter simultaneously with the rest of the boundary condition

Among them, the third approach will not be discussed at this place, because all of its details can be found in chapter 3.

With respect to the first approach, both curves in fig. 2.8 are based on the case of the 140 GHz gyrotron for *W7-X*, with a 40 GHz double-sided low-pass filter in ninth order. But one of them has $n = 0$ and the other $n = 3$, where n is the order of $\psi_n(t)$ which is defined as

$$\psi_n(t) = \mathcal{F}^{-1}\left\{ \frac{\omega^n}{\sqrt{\omega}^{\dagger}}\, h(\omega) \right\}$$

Signals in the future have negative time index, since the convolution afterwards will flip the function $\psi_n(t)$ around $t = 0$. If the future is ignored, the $n = 0$ case may still work, because the area between the curve and the x-axis for $t < 0$ is insignificant comparing with the area in the past ($t > 0$). But the curve for $n = 3$ is almost centred on the $t = 0$ axis. In this case, the future should not be omitted.

The second approach is shifting the original non-causal filter signal by Δt and omitting the rest insignificant part in the far future. The time shifting by Δt means multiplying its spectrum with $e^{j\omega\Delta t}$. The time delay will keep the amplitude of the

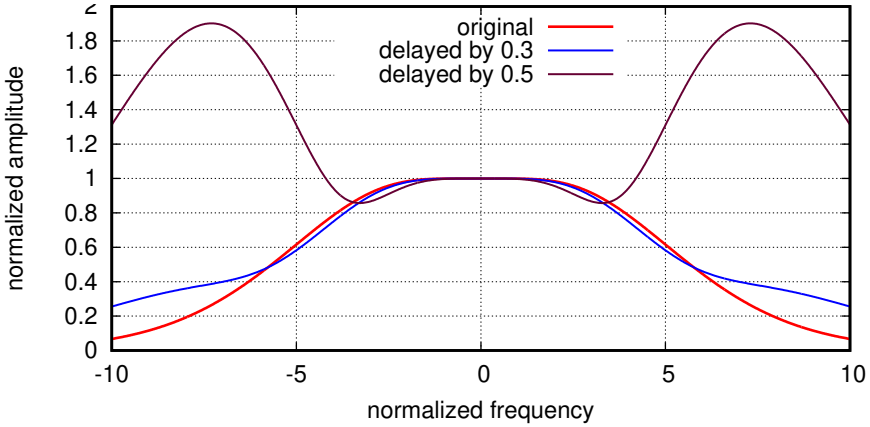

Fig. 2.9.: Filter in fifth order with normalized delay, phase compensated in third order

spectrum unmodified. However, it does not have zero phase inside the passing band any more. To compensate this effect, the polynomial will be extended through multiplying with a finite polynomial series of $e^{-j\omega\Delta t}$.

$$e^{-j\omega\Delta t} = 1 - j\Delta t\,\omega - \frac{\Delta t^2}{2}\omega^2 + j\frac{\Delta t^3}{6}\omega^3 + \mathcal{O}(\omega^4) \tag{2.44}$$

Fig. 2.9 shows the delayed and phase-compensated spectrum. All the units are normalized. Delays and compensations will firstly increase the aliasing effect by keeping the discretization of time unchanged. Secondly, a larger delay (e.g. the 0.5 time unit curve) may even cause the filter unstable, because it amplifies the band near the centre frequency.

Given the discussed limitations of the first two approaches, the third approach seems more promising. Details on its implementation will be described in chapter 3.5.2.

2.3. Solution II: Distribution

The inverse Fourier transform in (2.36) can be performed in the space of tempered distribution

$$\phi_n(t) := \mathcal{F}^{-1}\left\{\frac{\omega^n}{\sqrt{\omega}^\dagger}\right\} = \begin{cases} \dfrac{(1+j)\,j^n\,\Gamma(n+\frac{1}{2})}{\sqrt{\pi}\,t^{n+\frac{1}{2}}} & t>0 \\ 0 & t<0 \end{cases} \tag{2.45}$$

The transformed signal $\phi_n(t)$ is causal. However, except for $n=0$ this function is not improper integrable over the entire real axis, due to the singularity at $t=0$.

Hence, it can not be directly used in the convolution. To make use of the inverse Fourier in tempered distribution, the final convolution will be treated as a functional. Focusing on the convolution in (2.36)

$$\left\{ e^{-j\,\Delta\omega\, t}\mathcal{F}^{-1}\frac{\omega^n}{\sqrt{\omega}^\dagger} \;*\; \frac{\partial A(t)}{\partial z} \right\}(t) = \int_{-\infty}^{+\infty} \left\{ \mathcal{F}^{-1}\frac{(\omega+\Delta\omega)^n}{\sqrt{\omega+\Delta\omega}^\dagger} \right\}(\tau) \;\cdot\; \frac{\partial A}{\partial z}(t-\tau)\,\mathrm{d}\tau$$
$$= \left\langle \left\{ \mathcal{F}^{-1}\frac{(\omega+\Delta\omega)^n}{\sqrt{\omega+\Delta\omega}^\dagger} \right\}(\tau)\;,\; \frac{\partial A}{\partial z}(t-\tau) \right\rangle$$

By expanding the binomial term $(\omega+\Delta\omega)^n$ as

$$(\omega+\Delta\omega)^n = \omega^n + C_1\omega^{n-1}\Delta\omega + C_2\omega^{n-2}\Delta\omega^2 + \cdots$$

the last brackets can be written as

$$\left\langle \left\{ \mathcal{F}^{-1}\frac{(\omega+\Delta\omega)^n}{\sqrt{\omega+\Delta\omega}^\dagger} \right\}(\tau)\;,\; \frac{\partial A}{\partial z}(t-\tau) \right\rangle = \sum_{m=0}^{n} C_m \left\langle \left\{ \mathcal{F}^{-1}\frac{\omega^m}{\sqrt{\omega+\Delta\omega}^\dagger} \right\}(\tau)\;,\; \frac{\partial A}{\partial z}(t-\tau) \right\rangle$$

According to the properties of a distribution in (A.5) and (A.7), there is

$$\begin{aligned}
&\left\langle \left\{ \mathcal{F}^{-1}\frac{\omega^m}{\sqrt{\omega+\Delta\omega}^\dagger} \right\}(\tau)\;,\; \frac{\partial A}{\partial z}(t-\tau) \right\rangle \\
&= \left\langle \left(\frac{\partial}{j\,\partial\tau}\right)^m \left\{ \mathcal{F}^{-1}\frac{1}{\sqrt{\omega+\Delta\omega}^\dagger} \right\}(\tau)\;,\; \frac{\partial A}{\partial z}(t-\tau) \right\rangle \\
&= \left(-\frac{1}{j}\right)^m \left\langle \left\{ \mathcal{F}^{-1}\frac{1}{\sqrt{\omega+\Delta\omega}^\dagger} \right\}(\tau)\;,\; \left(\frac{\partial}{\partial\tau}\right)^m \frac{\partial A}{\partial z}(t-\tau) \right\rangle \\
&= \left(\frac{1}{j}\right)^m \left\langle \left\{ \mathcal{F}^{-1}\frac{1}{\sqrt{\omega+\Delta\omega}^\dagger} \right\}(\tau)\;,\; \left(\frac{\partial}{\partial(t-\tau)}\right)^m \frac{\partial A}{\partial z}(t-\tau) \right\rangle \\
&= \left(\frac{1}{j}\right)^m \left\langle e^{-j\,\Delta\omega\,\tau}\left\{ \mathcal{F}^{-1}\frac{1}{\sqrt{\omega}^\dagger} \right\}(\tau)\;,\; \left(\frac{\partial}{\partial(t-\tau)}\right)^m \frac{\partial A}{\partial z}(t-\tau) \right\rangle \\
&= \left(\frac{1}{j}\right)^m \left(e^{-j\,\Delta\omega\, t}\mathcal{F}^{-1}\frac{1}{\sqrt{\omega}^\dagger} \right) \;*\; \left(\frac{\partial}{\partial t}\right)^m \frac{\partial A}{\partial z}(t)
\end{aligned}$$

Defining

$$\hat{g}_n(t) \;:=\; \left(\frac{1}{j}\right)^n \left(e^{-j\,\Delta\omega\, t}\mathcal{F}^{-1}\frac{1}{\sqrt{\omega}^\dagger} \right) \;*\; \left(\frac{\partial}{\partial t}\right)^n \frac{\partial A}{\partial z}(t) \tag{2.46}$$

then (2.36) for z at boundary becomes

$$A(t) = \frac{1}{j\sqrt{2\pi}}\frac{c_0}{\sqrt{\omega_0+\omega_c}}\sum_{n=0} a_n\,\hat{g}_n(t) \tag{2.47}$$

where the coefficients a_n already include all of the polynomial coefficients' products. The inverse Fourier in $\hat{g}_n(t)$ is still a Fourier transform for tempered distributions. It can be calculated with help of Lebesgue's dominated convergence theorem and Fubini's theorem as the following improper integral

$$\mathcal{F}^{-1}\frac{1}{\sqrt{\omega}^{\dagger}} = \frac{1}{\sqrt{2\pi}} \lim_{a\to\infty} \lim_{b\to\infty} \int_{-a}^{b} \frac{1}{\sqrt{\omega}^{\dagger}}\, e^{j\omega t}\, \mathrm{d}\omega = \begin{cases} \dfrac{1+j}{\sqrt{t}} & t > 0 \\ 0 & t < 0 \end{cases} \tag{2.48}$$

This solution transforms the singularity of $\mathcal{F}^{-1}\frac{\omega^n}{\sqrt{\omega}^{\dagger}}$ into evaluating $\left(\frac{\partial}{\partial t}\right)^n \frac{\partial A(t)}{\partial z}$. However, $A(t)$ is a time discrete numerical function, so high order time derivatives may not be obtained accurately enough.

2.4. Summary

In this chapter, the essential equation (2.36) for a broadband boundary condition with user-defined, frequency-dependent reflection in time domain is defined. Two methods are proposed for solving this equation.

The first method performs the inverse Fourier transform in $\mathcal{L}^1$ space with help of an exponential filter. With this method, there is no singularity and the maximal time discretization for the boundary condition can be easily calculated. The estimation of the maximal allowed time discretization of the broadband boundary conditions is meaningful, since this value usually dominates the simulation's global time discretization. However the introduced filter should have zero-phase, which means it is a non-causal filter. Methods to circumvent the non-causality are discussed.

In the second method, the inverse Fourier transform is performed directly in the space of tempered distributions, by treating the final convolution as a linear functional. This method however requires time derivatives of $\frac{\partial A}{\partial z}$, which are numerical and therefore may be inaccurate at high orders.

In the next chapter, both methods will be used in several examples and their behaviour as well as suitability will be assessed.

3. Numerical implementation and validation

In a gyrotron the electromagnetic field is excited by the electron beam. However, in order to test the broadband boundary conditions without a possible RF noise due to the electrons and to be able also to feed the system with any arbitrary current excitations, a prototype program has been written during this master thesis. For simplicity, a straight homogeneous hollow waveguide is chosen as the test object. Current excitations can be placed at any user-defined positions inside this waveguide. Since the boundary conditions will be later integrated into the EURIDICE code, the same numerical schemes from EURIDICE are reimplemented in this test program to keep the compatibilities of equations

The default test scenario in this chapter is based on the configuration of the 140 GHz *W7-X* gyrotron, which is listed in table 3.1. Δt and Δz are the global time and spatial discretizations.

waveguide mode	waveguide radius	carrier frequency	cut-off frequency	Δt	Δz
$TE_{28,8}$	22.08 mm	140 GHz	129.875 GHz	1 ps	50 μm

Table 3.1.: Configuration of the default test scenario

Although only the homogeneous waveguides are tested, the same equations are also valid for more general waveguides, like mildly inhomogeneous resonators, where the z-dependency of the axial wavenumber $k_{\parallel}$ should be considered.

3.1. Slow time scale

As mentioned in the first chapter, the fields are separated into eigenmodes and there is a slow-time-scale assumption, which assumes that the mode-related envelope function

$A(z,t)$ changes slowly over the time, i.e. the spectrum of $A(z,t)$ has the maximal frequency ω_m and it is assumed $\omega_m \ll \omega_0$. This implies

$$\left|\frac{\partial A}{\partial t}\right| \ll \omega_0 \left|A\right| \tag{3.1}$$

consequently

$$\left|\frac{\partial^2 A}{\partial t^2}\right| \ll \omega_0 \left|\frac{\partial A}{\partial t}\right| \tag{3.2}$$

Combining the Maxwell's equations, results in the inhomogeneous Helmholtz equation with a current excitation J

$$\nabla^2 \mathbf{E} - \mu\epsilon \frac{\partial^2}{\partial t^2}\mathbf{E} = -\mu \frac{\partial}{\partial t}\mathbf{J} \tag{3.3}$$

Since the test waveguide is homogeneous, the z-dependency of $\mathbf{e}(r,\phi\,;z)$ in (2.12) does not exist

$$\mathbf{E} = A(z,t)\, e^{j\omega_0 t}\, \mathbf{e}(r,\phi)$$

Substituting $\mathbf{E}$ into the Helmholtz equation yields

$$\left(\frac{\partial^2}{\partial z^2} + \nabla_\perp^2\right)\left[A(z,t)\, e^{j\omega_0 t}\, \mathbf{e}(r,\phi)\right] - \mu\epsilon \frac{\partial^2}{\partial t^2}\left[A(z,t)\, e^{j\omega_0 t}\, \mathbf{e}(r,\phi)\right] = -\mu \frac{\partial}{\partial t}\mathbf{J}$$

Expanding the time derivative once

$$\begin{aligned}\frac{\partial^2 A(z,t)}{\partial z^2}\, e^{j\omega_0 t}\, \mathbf{e}(r,\phi) + A(z,t)\, e^{j\omega_0 t}\, \nabla_\perp^2 \mathbf{e}(r,\phi) \\ - \mu\epsilon \left\{\frac{\partial}{\partial t}\left(\frac{\partial A(z,t)}{\partial t}\, e^{j\omega_0 t} + j\omega\, A(z,t)\, e^{j\omega_0 t}\right)\right\}\mathbf{e}(r,\phi) = -\mu \frac{\partial}{\partial t}\mathbf{J}\end{aligned} \tag{3.4}$$

Extracting the term in the big brace and using (3.2)

$$\begin{aligned}\frac{\partial}{\partial t}\left(\frac{\partial A}{\partial t}\, e^{j\omega_0 t} + j\omega\, A\, e^{j\omega_0 t}\right) &= \left(\cancel{\frac{\partial^2 A}{\partial t^2}} + j\omega_0 \frac{\partial A}{\partial t} + j\omega_0 \frac{\partial A}{\partial t} - \omega_0^2 A\right) e^{j\omega_0 t} \\ &\approx \left(2j\omega_0 \frac{\partial A}{\partial t} - \omega_0^2 A\right) e^{j\omega_0 t}\end{aligned}$$

Since $\nabla_\perp^2 \mathbf{e}(r,\phi) + k_\perp^2 \mathbf{e}(r,\phi) = 0$ and $k_\parallel^2 = \mu\epsilon\,\omega^2 - k_\perp^2$, choosing

$$\mathbf{J} = J(z,t)\, \mathbf{e}(r,\phi) \tag{3.5}$$

(3.4) can be reduced to a scalar equation

$$\frac{\partial^2 A}{\partial z^2} + k_0^2\, A - 2j\omega_0\, \mu\epsilon\, \frac{\partial A}{\partial t} = -\mu \frac{\partial J}{\partial t}\, e^{-j\omega_0 t} \tag{3.6}$$

k_0 denotes the $k_\parallel$ at ω_0, i.e. $k_0^2 = \mu\epsilon\,\omega_0^2 - k_\perp^2$. For a TE-mode in a conventional cylindrical waveguide, $k_\perp = \frac{\chi}{R}$, where χ is a root of the first derivative of the Bessel function and R is the radius of the waveguide.

3.2. Excitations (source terms)

The waveguide in (3.6) is excited through the mode-relevant current density $J(z,t)$. Instead of the electron movement in a real gyrotron, it is assumed that the current excitation is placed only at one dedicated position z_0 and does not move. Then, only the time dependency of the current needs to be studied. There are three kinds of current sources implemented in this code:

1. an harmonic excitation at the carrier frequency ω_0
2. arbitrary number of harmonic excitations at any discrete frequencies
3. Gaussian impulses

Single frequency source

An excitation at one single frequency ω at the position z_0, has the form

$$J(z,t) = e^{j\omega t}\,\delta(z-z_0)$$

The right-hand side of (3.6) is then

$$-\mu\frac{\partial J}{\partial t}\,e^{-j\omega_0 t} = -j\omega\,\mu\,e^{j(\omega-\omega_0)t}\,\delta(z-z_0) \tag{3.7}$$

A special case is when the frequency of $J(t)$ equals to the carrier. The right-hand side of (3.6) reduces to a constant in time

$$-\mu\frac{\partial J}{\partial t}\,e^{-j\omega_0 t} = -j\omega_0\,\mu\,\delta(z-z_0) \tag{3.8}$$

Gaussian impulse

A Gaussian impulse has an infinitely broad spectrum. But the most power is centralized on the frequency band spectrally around the frequency $\omega_z \in \mathbb{R}$ in the form of a Gaussian distribution. The inverse Fourier transform of this spectrum still keeps its amplitude in a Gaussian distribution:

$$\hat{J}(z,\omega) \;=\; e^{-\frac{(\omega-\omega_z)^2}{\Omega}}\,\delta(z-z_0) \quad \text{with } \Omega \in \mathbb{R}^+ \tag{3.9a}$$

$$\updownarrow$$

$$\mathcal{F}^{-1}\left\{\hat{J}(z,\omega)\right\} \;\propto\; e^{-\frac{\Omega}{4}t^2}\,e^{j\omega_z t}\,\delta(z-z_0) \tag{3.9b}$$

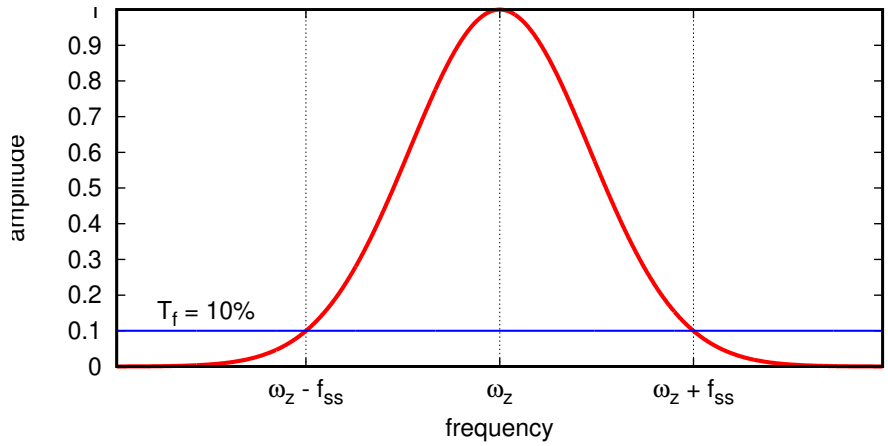

Fig. 3.1.: Cropping the Gaussian impulse in frequency domain

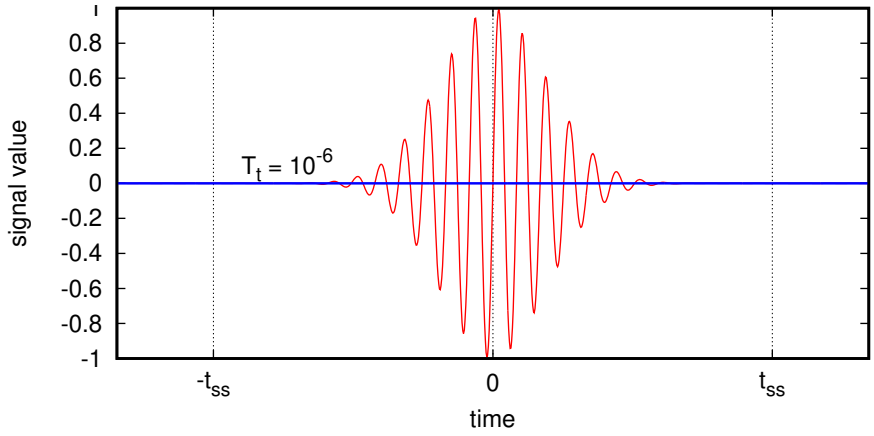

Fig. 3.2.: Cropping the Gaussian impulse in time domain

The signal in time domain (3.9b) is intentionally normalized on unity.

Since the Gaussian impulse is infinite along both frequency and time axis, it has to be cropped in the real applications. Two thresholds T_f and T_t are defined for the limitation of frequency and time. The spectrum will be omitted, when its amplitude is below T_f. Similarly, in time domain, the signal will be ignored at time instances where its amplitude its less than T_t. By default T_f is chosen 10% of the maximum i.e. $-20\,\mathrm{dB}$ and $T_t = 10^{-6}$. This concept is presented in fig. 3.1 and fig. 3.2 . The variable f_{ss} denotes the single-sided bandwidth, which is given by the user as an input parameter. Estimation of Ω in (3.9) relies on this input. The single side time duration t_{ss} tells the program, that this source should be excited twice long as t_{ss}. Ω and t_{ss} are calculated by

$$\Omega = -\frac{(2\pi f_{\mathrm{ss}})^2}{\ln T_f} \tag{3.10}$$

and

$$t_{\mathrm{ss}} = \sqrt{-\frac{4 \ln T_t}{\Omega}} \tag{3.11}$$

Delaying a signal does not change its spectral amplitude. So the current density in (3.9b) will be delayed by t_{ss} for convenience.

$$-\mu \frac{\partial J}{\partial t} e^{-j\omega_0 t} = \mu \left(-\frac{\Omega}{2}(t - t_{\mathrm{ss}}) + j\omega_z \right) e^{-\frac{\Omega}{4}(t-t_{\mathrm{ss}})^2} e^{j(\omega_z - \omega_0)(t-t_{\mathrm{ss}})} \delta(z - z_0) \tag{3.12}$$

This is the Gaussian source used in (3.6).

3.3. Numerical methods

The boundary condition used in this test program[1] is formulated as

$$\left. \frac{\partial A(z,t)}{\partial z} \right|_{z \to z_b} = X_1 \, A(z_b, t) + X_2 \tag{3.13}$$

where z_b is the z-coordinate at the boundary. X_1 and X_2 will be the results returned from the subroutines for calculation of the boundary status. For the usual single-frequency matched boundary condition in (2.20), there is $X_2 = 0$ and

$$X_1 = \begin{cases} jk_{\parallel} \, Z & \text{left (gun) side} \\ -jk_{\parallel} \, Z & \text{right (launcher) side} \end{cases}$$

with the wave-impedance

$$Z = \frac{1 - \Gamma}{1 + \Gamma}$$

Now (3.13) will be embedded into the numerical equations. In the following, Δz is used for the spatial discretization length, Δt for the duration of each time interval and k_0 is the axial wavenumber $k_{\parallel}$ at frequency ω_0. Letters z and t stand for discrete counters of spatial segment and time interval, respectively. Notation A_z^t means the value of the envelope function at $t \cdot \Delta t$ time and $z \cdot \Delta z$ position. f_z^t stands for the source on the right-hand side of (3.6).

For the numerical implementation of the equations (3.6) and (3.13), two numerical schemes are used, as described below.

[1] also in EURIDICE

The fully implicit scheme

After applying the implicit finite difference scheme (also called BTCS scheme, see [11]), (3.6) corresponds to

$$\frac{1}{\Delta z^2}\left(A_{z-1}^{t+1} - 2A_z^{t+1} + A_{z+1}^{t+1}\right) + k_0^2\, A_z^{t+1} - j\frac{2\omega_0\mu\epsilon}{\Delta t}\left(A_z^{t+1} - A_z^t\right) = -f_z^t$$

Variables at the time step $t+1$ are unknown. Sorting the known variables to the left side and the unknowns to the right side, results in the following vector equation

$$\left(\frac{1}{\Delta z^2}\ ,\ k_0^2 - \frac{2}{\Delta z^2} - j\frac{2\omega_0\mu\epsilon}{\Delta t}\ ,\ \frac{1}{\Delta z^2}\right)\begin{pmatrix} A_{z-1}^{t+1} \\ A_z^{t+1} \\ A_{z+1}^{t+1} \end{pmatrix} = -j\frac{2\omega_0\mu\epsilon}{\Delta t}\, A_z^t - f_z^t \tag{3.14}$$

Applying the same rule on (3.13), yields for the boundary on the left-hand side (which has a smaller z coordinate than the boundary on the right-hand side of the waveguide)

$$\left(k_0^2 - \frac{2}{\Delta z^2} - j\frac{2\omega_0\mu\epsilon}{\Delta t} - \frac{2X_1}{\Delta z}\ ,\ \frac{2}{\Delta z^2}\right)\begin{pmatrix} A_z^{t+1} \\ A_{z+1}^{t+1} \end{pmatrix} = -j\frac{2\omega_0\mu\epsilon}{\Delta t}A_z^t - f_z^t + \frac{2X_2}{\Delta z} \tag{3.15}$$

and for the boundary on the right-hand side

$$\left(\frac{2}{\Delta z^2}\ ,\ k_0^2 - \frac{2}{\Delta z^2} - j\frac{2\omega_0\mu\epsilon}{\Delta t} + \frac{2X_1}{\Delta z}\right)\begin{pmatrix} A_{z-1}^{t+1} \\ A_z^{t+1} \end{pmatrix} = -j\frac{2\omega_0\mu\epsilon}{\Delta t}A_z^t - f_z^t - \frac{2X_2}{\Delta z} \tag{3.16}$$

Concatenating these three vector equations at every z-position together, a matrix equation can be built, which transforms the system to a classical $Ax = b$ problem. Furthermore, the matrix A is tridiagonal. Therefore, the equation can be solved efficiently by the Thomas algorithm [12]. This scheme is 1^{st} order accurate in time and 2^{nd} order accurate in space.

The Crank-Nicolson scheme

Also the Crank-Nicolson method [12] is implemented in the code. It has second-order convergence in time. In this method the equations are shifted by $\frac{\Delta t}{2}$ through averaging the variables at t and $t + \Delta t$. Shifting (3.6) to $t + \frac{\Delta t}{2}$ yields

$$\frac{1}{2\Delta z^2}\left(A_{z+1}^{t+1} - 2A_z^{t+1} + A_{z-1}^{t+1} + A_{z+1}^t - 2A_z^t + A_{z-1}^t\right) + \frac{k_0^2}{2}\left(A_z^{t+1} + A_z^t\right) - j\frac{2\omega_0\mu\epsilon}{\Delta t}\left(A_z^{t+1} - A_z^t\right) = -f_z^{t+\cancel{\frac{1}{2}}}$$

The time shifting on f_z^t is cancelled since the absolute time is not important. After separating of knowns and unknowns, there is the vector equation

$$\left(\frac{1}{2\Delta z^2}\ ,\ \frac{k_0^2}{2}-\frac{1}{\Delta z^2}-j\frac{2\omega_0\mu\epsilon}{\Delta t}\ ,\ \frac{1}{2\Delta z^2}\right)\begin{pmatrix} A_{z-1}^{t+1} \\ A_z^{t+1} \\ A_{z+1}^{t+1} \end{pmatrix}$$
$$=-\left(\frac{1}{2\Delta z^2}\ ,\ \frac{k_0^2}{2}-\frac{1}{\Delta z^2}+j\frac{2\omega_0\mu\epsilon}{\Delta t}\ ,\ \frac{1}{2\Delta z^2}\right)\begin{pmatrix} A_{z-1}^{t} \\ A_z^{t} \\ A_{z+1}^{t} \end{pmatrix}-f_z^t \quad (3.17)$$

Shifting the boundary equations (3.13) by $\frac{\Delta t}{2}$ results in

$$\left(\frac{k_0^2}{2}-\frac{1}{\Delta z^2}-j\frac{2\omega_0\mu\epsilon}{\Delta t}-\frac{X_1}{\Delta z}\ ,\ \frac{1}{\Delta z^2}\right)\begin{pmatrix} A_z^{t+1} \\ A_{z+1}^{t+1} \end{pmatrix}$$
$$=-\left(\frac{k_0^2}{2}-\frac{1}{\Delta z^2}+j\frac{2\omega_0\mu\epsilon}{\Delta t}-\frac{X_1}{\Delta z}\ ,\ \frac{1}{\Delta z^2}\right)\begin{pmatrix} A_z^{t} \\ A_{z+1}^{t} \end{pmatrix}-f_z^t+\frac{2X_2}{\Delta z} \quad (3.18)$$

for the boundary on the left-hand side of the waveguide. Whereas, for the right-hand side

$$\left(\frac{1}{\Delta z^2}\ ,\ \frac{k_0^2}{2}-\frac{1}{\Delta z^2}-j\frac{2\omega_0\mu\epsilon}{\Delta t}+\frac{X_1}{\Delta z}\right)\begin{pmatrix} A_{z-1}^{t+1} \\ A_z^{t+1} \end{pmatrix}$$
$$=-\left(\frac{1}{\Delta z^2}\ ,\ \frac{k_0^2}{2}-\frac{1}{\Delta z^2}+j\frac{2\omega_0\mu\epsilon}{\Delta t}+\frac{X_1}{\Delta z}\right)\begin{pmatrix} A_{z-1}^{t} \\ A_z^{t} \end{pmatrix}-f_z^t-\frac{2X_2}{\Delta z} \quad (3.19)$$

These equations build up again an $Ax = b$ problem with a tridiagonal matrix A.

Examples

Both the Crank-Nicolson scheme and the fully implicit scheme give the same result under non-critical time and spatial discretizations. Fig. 3.3 demonstrates a Gaussian impulse excited at one point in the centre of a wave guide and travelling towards the boundaries. These figures are calculated through the above mentioned equation systems with matched boundary conditions on both sides. (Details on the implementation of the boundary conditions will be given in the next sections.)

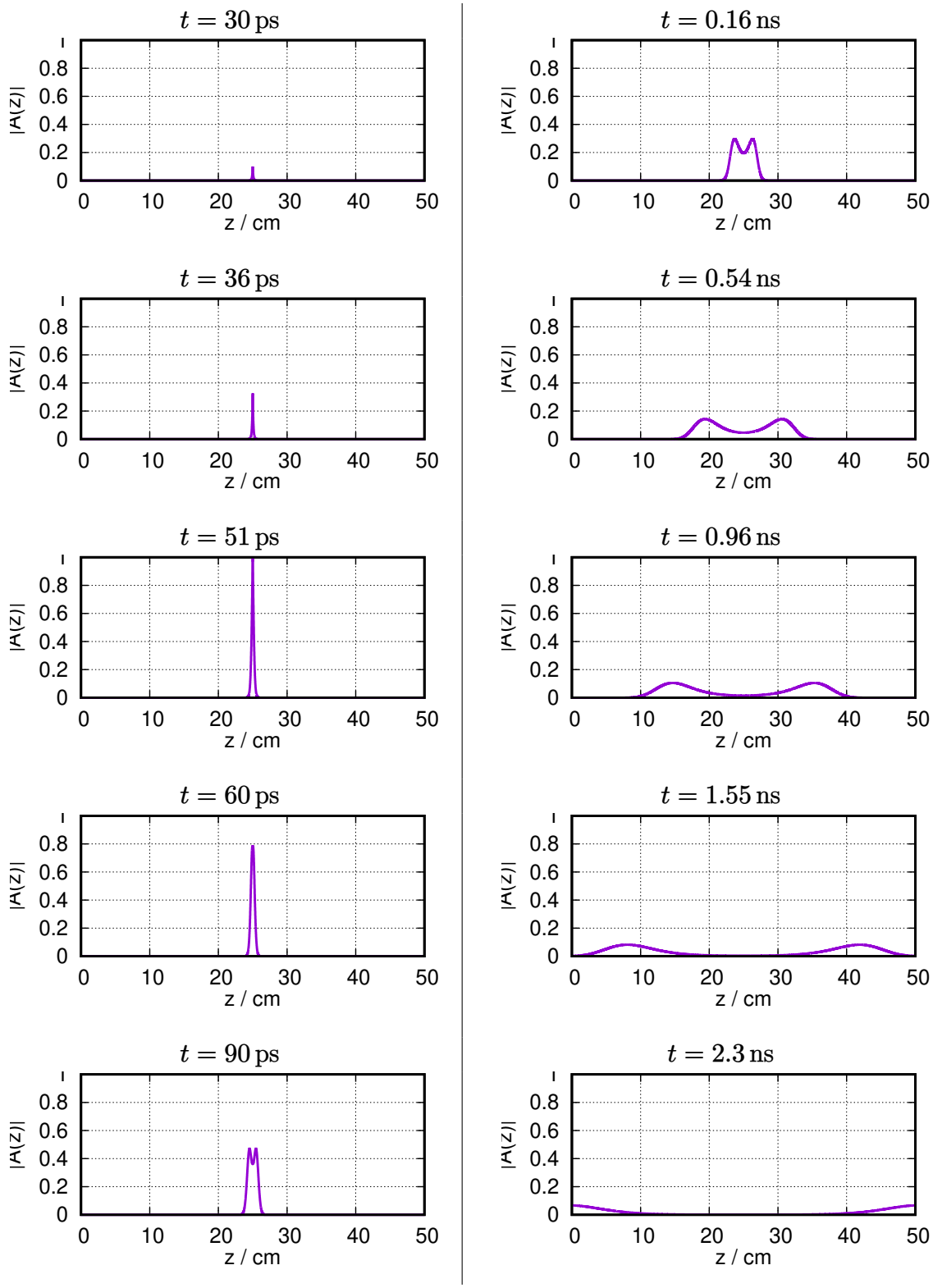

Fig. 3.3.: Demonstration of the time dependent envelope function by a point Gaussian excitation in the middle of a homogeneous waveguide

3.4. Single-frequency matched boundary condition

The single-frequency matched boundary condition will be tested first, in order to verify the code and to compare with the result of the broadband boundary condition later. This boundary condition has the form

$$A(z,t) = \frac{s}{jk_0}\frac{\partial A(z,t)}{\partial z}$$

$s = \pm 1$ depending on the side. As shown in [13, 14], this boundary condition introduces a reflection

$$\Gamma(\omega) = \frac{k_\parallel(\omega) - k_0}{k_\parallel(\omega) + k_0} \tag{3.20}$$

At $k_\parallel = k_0$ (i.e. $\omega = \omega_0$) there is zero reflection. The code reproduces exactly this theoretical result as shown in the following tests.

Testing with discrete frequencies

Still taking the 140 GHz gyrotron case as an example ($\omega_0 = 2\pi \times 140\,\mathrm{GHz}$), several signals with different frequencies are excited. Because of the linearity of the system, it does not matter, whether the signals are excited at once or every simulation only handles one frequency. Since the frequencies are defined discretely, rather than a diagram for the whole sparse frequency band, table 3.2 shows the reflection coefficients only at the defined frequencies. The numerical results coincide the theoretical values.

freq.	simulated		theoretical	
GHz	$\lvert\Gamma\rvert$	$\arg(\Gamma)/^\circ$	$\lvert\Gamma\rvert$	$\arg(\Gamma)/^\circ$
120	1	−92.86	1	−92.92
125	1	−112.59	1	−112.01
133	0.298	−177.65	0.292	180
138	0.055	180	0.057	180
140	0	-	0	-
142	0.046	0	0.047	0
147	0.138	0	0.137	0
160	0.283	0	0.283	0

Table 3.2.: Numerical results of the single-frequency boundary condition

Testing with a broadband Gaussian impulse

The same waveguide and boundary condition will be tested now under a Gaussian impulse source. The spectrum of the Gaussian source is centred at 150 GHz and has a single-side bandwidth of 30 GHz. This means, the source covers from 120 GHz to 180 GHz and the signal strength at these two frequencies is 20 dB weaker than the component at 150 GHz (see fig. 3.1). The reflection coefficient excited by a Gaussian pulse is plotted in fig. 3.4. As it can be seen, this boundary condition has zero reflection only at the carrier frequency 140 GHz. Nevertheless, the simulated reflection is identical with the theoretical one in (3.20), which verifies the correctness of the implementation.

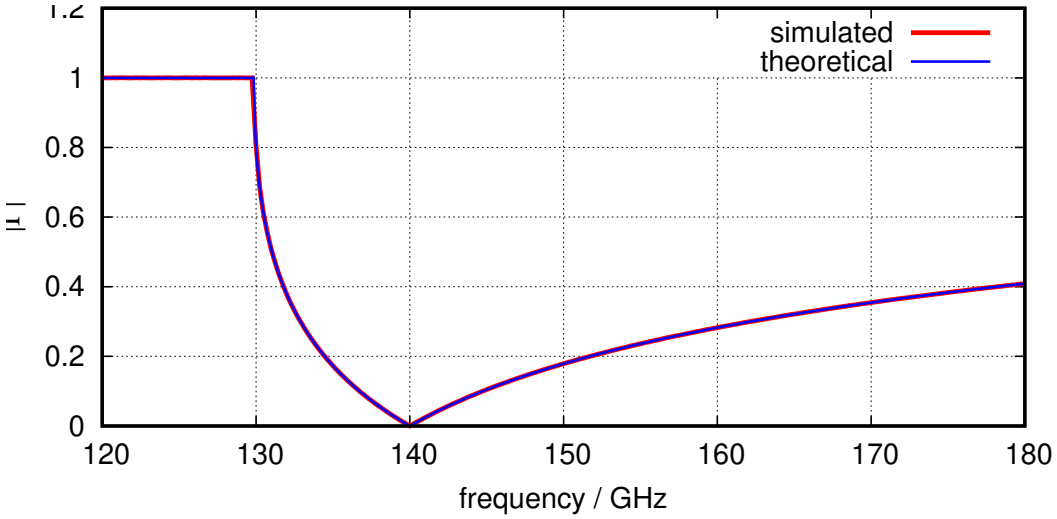

Fig. 3.4.: Reflection coefficient for the single-frequency boundary condition

3.5. Broadband boundary condition

As can be seen in the previews section, with the single-frequency boundary condition there is only one frequency that is really matched. The range of the matched frequencies can be extended by using the formulation of the broadband boundary condition described in chapter 2.1.4. In addition, a user-defined reflection different from zero can be introduced.

3.5.1. Implementation of the solution in the space of tempered distributions

As (2.47) shows, the broadband boundary condition in tempered distribution is

$$A(t) = \frac{c_0}{\sqrt{\omega_0 + \omega_c}} \frac{1}{j\sqrt{2\pi}} \left(e^{j\,\Delta\omega\, t}\ \mathcal{F}^{-1} \frac{1}{\sqrt{\omega}^{\dagger}} \right) * \underbrace{\left(\sum_{n=0}^{N} a_n \left(\frac{\partial}{\partial t} \right)^n \frac{\partial A}{\partial z}(t) \right)}_{=:\,\phi(t)} \tag{3.21}$$

Performing the inverse Fourier transform according to (2.48), despite the singularity at $t = 0$ which has to be integrated improperly, the signal itself is causal. So only the integral over the positive axis remains from the convolution , which yields

$$A(t) = \frac{1-j}{\sqrt{2\pi}} \frac{c_0}{\sqrt{\omega_0 + \omega_c}} \int_0^{\infty} \frac{e^{-j\,\Delta\omega\,\tau}}{\sqrt{\tau}}\, \phi(t-\tau)\, \mathrm{d}\tau$$

The function $\phi(t)$ represents the last part of (3.21). Assuming ϕ starts from the zero state i.e. $\phi(t) = 0$ for $t < t_0$, the code does not need to query the signal value in the infinite past.

$$A(t) = \frac{1-j}{\sqrt{2\pi}} \frac{c_0}{\sqrt{\omega_0 + \omega_c}} \int_0^{t-t_0} \frac{e^{-j\,\Delta\omega\,\tau}}{\sqrt{\tau}}\, \phi(t-\tau)\, \mathrm{d}\tau \tag{3.22}$$

Since $\phi(t-\tau)$ is numerically defined at discrete points of time, (3.22) can not be calculated further through the analytical way. The best solution is to interpolate ϕ and do this integral carefully. But that is not necessary for the first approximation. In the present code, (3.22) is evaluated by the approximation (the same as in EURIDICE):

$$A(t) \approx \frac{1-j}{\sqrt{2\pi}} \frac{c_0}{\sqrt{\omega_0 + \omega_c}} \sum_n \left(\frac{\phi(t-\tau_n) + \phi(t-\tau_{n+1})}{2} \int_{\tau_n}^{\tau_{n+1}} \frac{e^{-j\,\Delta\omega\,\tau}}{\sqrt{\tau}}\, \mathrm{d}\tau \right) \tag{3.23}$$

where

$$\int_{\tau_n}^{\tau_{n+1}} \frac{e^{-j\,\Delta\omega\,\tau}}{\sqrt{\tau}}\, \mathrm{d}\tau = \int_0^{\tau_{n+1}} \frac{e^{-j\,\Delta\omega\,\tau}}{\sqrt{\tau}}\, \mathrm{d}\tau - \int_0^{\tau_n} \frac{e^{-j\,\Delta\omega\,\tau}}{\sqrt{\tau}}\, \mathrm{d}\tau$$

and

$$\int_0^t \frac{e^{-j\,\Delta\omega\,\tau}}{\sqrt{\tau}}\, \mathrm{d}\tau = \frac{2}{\sqrt{j\,\Delta\omega}} \int_0^t e^{-j\,\Delta\omega\,\tau}\, \mathrm{d}\sqrt{j\,\Delta\omega\,\tau} = \sqrt{\frac{\pi}{j\,\Delta\omega}}\, \mathrm{erf}(\sqrt{j\,\Delta\omega\, t})$$

This complex error function can be decomposed into the Fresnel integrals (used in EURIDICE and [14] as well), which results in

$$\int_0^t \frac{e^{-j\,\Delta\omega\,\tau}}{\sqrt{\tau}}\, \mathrm{d}\tau = \sqrt{\frac{2\pi}{\Delta\omega}} \left\{ \mathrm{C}\left(\sqrt{\frac{2}{\pi}\,\Delta\omega\, t} \right) - j\mathrm{S}\left(\sqrt{\frac{2}{\pi}\,\Delta\omega\, t} \right) \right\} \quad \text{for } \Delta\omega > 0 \tag{3.24}$$

$\mathrm{C}(x)$ and $\mathrm{S}(x)$ are the Fresnel integrals, which are defined as

$$\mathrm{C}(x) = \int_0^x \cos(t^2)\,\mathrm{d}t \tag{3.25a}$$

$$\mathrm{S}(x) = \int_0^x \sin(t^2)\,\mathrm{d}t \tag{3.25b}$$

The time differentiation is done numerically by the finite difference:

$$\frac{\partial}{\partial t}\frac{\partial A}{\partial z}(t) = \frac{\frac{\partial A}{\partial z}(t) - \frac{\partial A}{\partial z}(t-\Delta t)}{\Delta t} \tag{3.26a}$$

$$\left(\frac{\partial}{\partial t}\right)^2\frac{\partial A}{\partial z}(t) = \frac{\frac{\partial}{\partial t}\frac{\partial A}{\partial z}(t) - \frac{\partial}{\partial t}\frac{\partial A}{\partial z}(t-\Delta t)}{\Delta t} \tag{3.26b}$$

...

In the first order, this one-sided finite difference is also compatible with the Crank-Nicolson method, as it becomes automatically a two-sided numerical derivative around the time $t - \frac{\Delta t}{2}$. So far (3.22) is completely solved and can be transformed into the form of (3.13).

In the following, the broadband boundary condition is tested for the matched case (ideally it would be zero reflection at any frequency) and without any polynomial compensation (zero order). This means, $a_0 = \pm 1$, $a_1 = 0$ and (3.22) reduces to

$$A(t) = \pm\frac{1-j}{\sqrt{2\pi}}\frac{c_0}{\sqrt{\omega_0+\omega_c}}\int_0^{t-t_0}\frac{e^{-j\,\Delta\omega\,\tau}}{\sqrt{\tau}}\,\frac{\partial A}{\partial z}(t-\tau)\,\mathrm{d}\tau \tag{3.27}$$

The sign depends on the side of the boundary: plus for the boundary on the left-hand side, whereas minus for the right-hand side.

Testing with discrete frequencies

Table 3.3 shows the simulated result with excitations in discrete frequencies. k_3 (see chapter 2.1.3) is used as the axial wavenumber, without any polynomial compensation. It can be proven in a similar way as in [13], that the zero-order matched broadband boundary condition (3.27) has a theoretical reflection of

$$\Gamma(\omega) = \frac{k_\parallel(\omega) - k_3(\omega)}{k_\parallel(\omega) + k_3(\omega)} \tag{3.28}$$

It differs from zero because of the approximation (2.25) for $k_\parallel$. As it can be seen, that the amplitude differences of the defined frequencies are not larger than 4 dB, except at the carrier frequency at 140 GHz. The non-zero reflection at the carrier frequency is caused by the accuracy level of the discrete Fourier transform. The leading negative sign of the dB values is self-evident, therefore it is omitted.

Testing with a broadband Gaussian impulse

Again a Gaussian impulse from 120 GHz to 180 GHz is fed into the default waveguide. Its reflection coefficient over the entire frequency band is shown in fig. 3.5. The reflection coefficients are not absolute zero and the farther from the carrier, the higher is the reflection. The simulation is a bit worse than the theoretical curve, but they are all in a very low range. Besides, there is a discontinuity at the cut-off frequency 129.9 GHz, since at that frequency the axial wavenumber $k_\parallel$ in the denominator equals to zero. There is a comparison between this broadband boundary condition and the single-frequency one in fig. 3.6. The broadband boundary condition has about 20 dB less reflection, when looking at the whole frequency band.

The above examples show that the implementation of the broadband boundary condition using the tempered distribution approach works very well in the matched, zero reflection case. This is the actually state-of-the-art for the broadband boundary condition in EURIDICE and [14]. The advantage of the formulation (3.21) compared to the state-of-the-art formulation lies in two aspects:

1. Using the Polynomial compensation, the matched boundary condition can be improved further.
2. A user-defined, non-zero reflection can be treated.

These aspects will be discussed in chapter 3.6.

3.5.2. Implementation of the solution in the space of Lebesgue integrable functions

The broadband boundary condition (2.37) in the Lebesgue integrable space is formulated as

$$A(t) = \frac{c_0}{\sqrt{\omega_0 + \omega_c}} \frac{1}{\sqrt{2\pi}} \left(e^{-j\,\Delta\omega\, t}\ \mathcal{F}^{-1} g \right) * \frac{\partial A}{\partial z}(t)$$

where $g \in \mathcal{L}(\mathbb{R})$, its definition can be found in (2.42). Defining the abbreviation

$$\tilde{g}(t) := \frac{c_0}{\sqrt{\omega_0 + \omega_c}} \frac{1}{\sqrt{2\pi}} \left(e^{-j\,\Delta\omega\, t}\ \mathcal{F}^{-1} g \right) \tag{3.29}$$

the last equation becomes

$$A(t) = \tilde{g}(t) * \frac{\partial A}{\partial z}(t) = \int_{-\infty}^{\infty} \tilde{g}(t-\tau)\ \frac{\partial A}{\partial z}(\tau)\ \mathrm{d}\tau \tag{3.30}$$

frequency	/ GHz	120	125	133	138
simulated $\|\Gamma\|$	/ dB (neg.)	35.63	36.30	42.78	58.70
theoretical $\|\Gamma\|$	/ dB (neg.)	34.31	36.90	43.65	54.61
frequency	/ GHz	140	142	147	160
simulated $\|\Gamma\|$	/ dB (neg.)	64.81	52.22	44.32	33.20
theoretical $\|\Gamma\|$	/ dB (neg.)	∞	54.68	43.87	34.96

Table 3.3.: Results of the zero-order matched broadband boundary condition solved as a tempered distribution excited with discrete frequencies

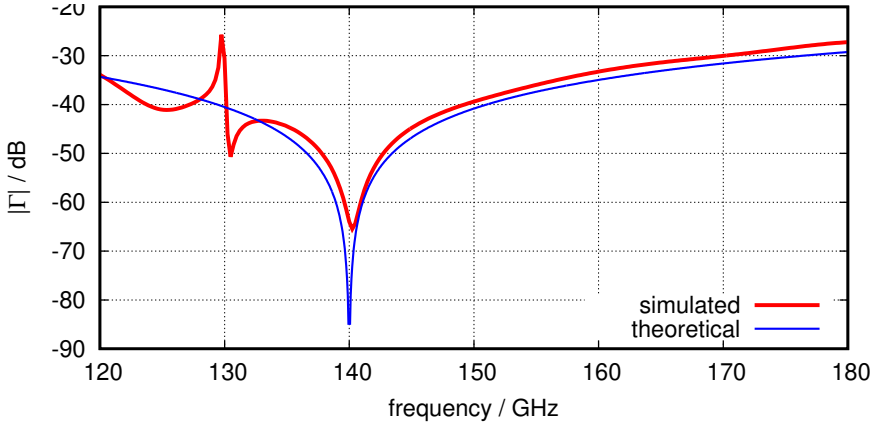

Fig. 3.5.: Results of the zero-order matched broadband boundary condition solved as a tempered distribution with a broadband excitation

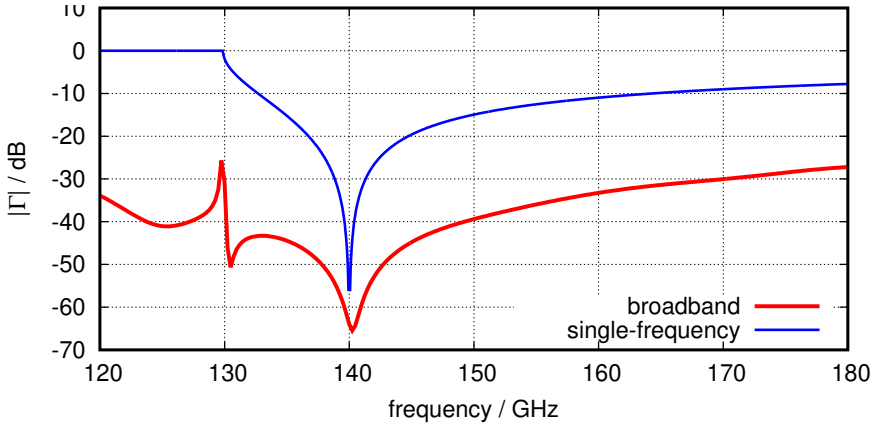

Fig. 3.6.: Comparison between the zero-order matched broadband boundary condition and single-frequency boundary conditions

Fig. 3.7 shows the typical behaviour of $\tilde{g}(t)$. The two time variables t_p and t_f are introduced. They denote the time duration of the most effective part in the past and future. t_f is the time in the future, where the filter signal "disappears". t_p is either the threshold of the filter signal or the starting time of the function $A(t)$, depending on which one is larger. Consequently, the convolution in (3.30) is approximated by

$$A(t) \approx \int_{t-t_p}^{t+t_f} \tilde{g}(t-\tau)\, \frac{\partial A}{\partial z}(\tau)\, \mathrm{d}\tau \tag{3.31}$$

Firstly, it has been tried to delay the convolution (3.31) into the past, so that the most effective interval (from $-t_f$ to t_p) is shifted in the past. This is done by substituting t with $t - t_f$, as (3.32) shows.

$$A(t-t_f) \approx \int_{t-t_p-t_f}^{t} \tilde{g}(t-\tau)\, \frac{\partial A}{\partial z}(\tau)\, \mathrm{d}\tau \tag{3.32}$$

This is the 3$^{\mathrm{rd}}$ approach mentioned in chapter 2.2 to circumvent the non-causality. The only unknown to be solved in (3.32) is the variable $\frac{\partial A}{\partial z}$ at the current time t. When this happens, X_1 in (3.13) is zero. This implies an explicit, rather than implicit, calculation.

Unfortunately (3.32) does not work, no matter how big t_f is chosen. The reason is probably its explicitness, which may require an extraordinary and totally impractical short time-step.

Another possibility to solve (3.31) is the ignorance of the future (the 1$^{\mathrm{st}}$ approach discussed in chapter 2.2). When $t_f = 0$, (3.31) reduces to

$$A(t) \approx \int_{t-t_p}^{t} \tilde{g}(t-\tau)\, \frac{\partial A}{\partial z}(\tau)\, \mathrm{d}\tau \tag{3.33}$$

Taking a seventh order filter (see fig. 2.6), again with zero-order impedance matching ($Z = 1$ in equation 2.10) as an example, fig. 3.8 shows the comparison of $\tilde{g}(t)$ with different filter bandwidths. As it can be seen, after 0.02 ns there is no difference between all of the low-pass filters. The broader bandwidth this filter has, the more "causal" it will be. It is expected that the signal of a filter with an infinite bandwidth in the time domain converges to the signal from the inverse Fourier in the space of tempered distributions.

By omitting the future, how the causality of the filter influences its reflection coefficient is presented in fig. 3.9. Also the same Gaussian impulse from 120 GHz to 180 GHz is excited in the waveguide. The reflection coefficient shows, that when the values in the future are ignored, a broadband filter has better matching than a narrow band one.

This is because the causality is related to the bandwidth of the filter. The properties of the solution with this approach, should be the same as the solution in the space of Lebesgue integrable functions, when the filter bandwidth is broad enough.

However, it has been observed that the non-causality of the zero-order filter can be compensated with an equivalent constant. This phenomenon will keep the system causal even under a filter with relative narrow bandwidth. This is a matter for further investigation, beyond the time-frame of the present thesis.

3.6. Making use of the polynomial series to advance the state-of-the-art

The most exciting features introduced by the presented formulations of boundary condition are the possibilities to set up a user-defined frequency-dependent complex reflection coefficient and to improve the existing zero-order matched boundary condition, which is currently the state-of-the-art. These possibilities correspond to the polynomial of the wave-impedance Z in (2.10) and the polynomial of the axial wavenumber $k_{\parallel}$ in (2.31), respectively. Both polynomials are merged together in the end.

In order to avoid the problem of the non-causality discussed earlier, the solution in the space of tempered distributions is used for testing the effect of these polynomials. As mentioned in chapter 3.5.1, the first order time derivative of $\frac{\partial A}{\partial z}(t)$ is accurately defined both for the implicit finite difference scheme and for the Crank-Nicolson scheme. Starting from second order, the time derivatives become less accurate. Their accuracy depends on the global time discretization. For this reason, in case higher-order polynomials appear in the boundary condition, they may cause numerical **instabilities**. As a consequence, only the first order polynomial will be tested. In other words, the relation in the frequency domain will be

$$\hat{A}(z,\omega) = \frac{c_0}{\sqrt{\omega_0+\omega_c}} \frac{1}{\sqrt{\omega+\Delta\omega}^{\dagger}} \left(a_0 + a_1\omega\right) \frac{\partial \hat{A}(z,\omega)}{\partial z} \tag{3.34}$$

In the time domain, (3.21) is reduced to

$$A(t) = \frac{c_0}{\sqrt{\omega_0+\omega_c}} \frac{1}{\sqrt{2\pi}} \left(e^{j\,\Delta\omega\, t}\; \mathcal{F}^{-1} \frac{1}{\sqrt{\omega}^{\dagger}} \right) * \left(a_0 \frac{\partial A}{\partial z}(t) - a_1 j \frac{\partial}{\partial t} \frac{\partial A}{\partial z}(t) \right) \tag{3.35}$$

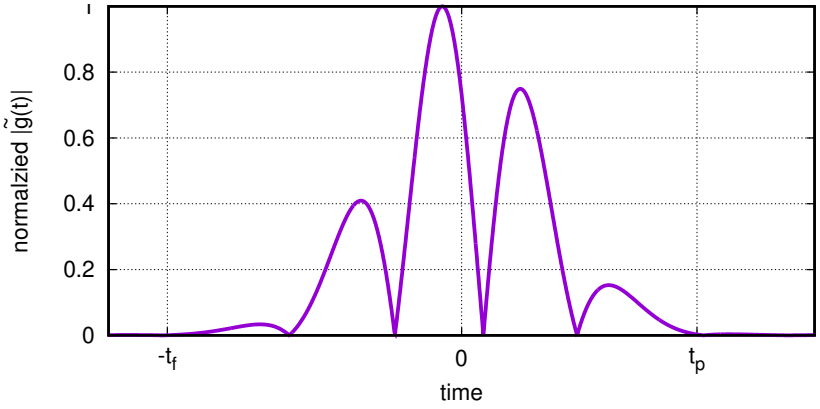

Fig. 3.7.: The typical behaviour of high order $\tilde{g}(t)$ with the introduction of t_p and t_f, see (3.29), $N = 3$ in (2.42)

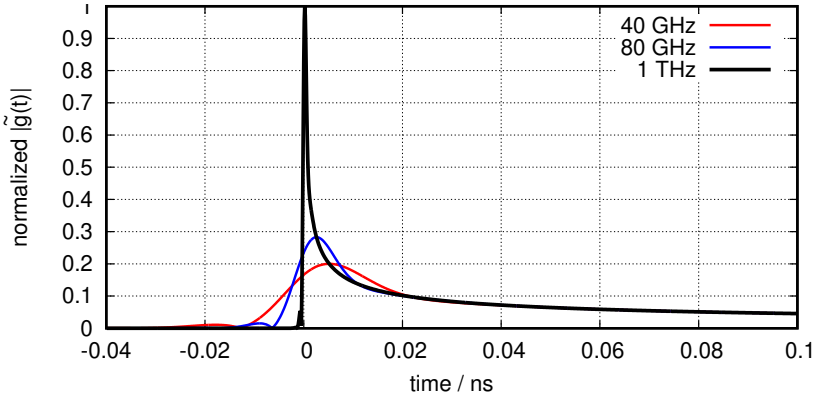

Fig. 3.8.: Comparison of zero-order matched $\tilde{g}(t)$ (which has a seventh order filter) for different double side filter bandwidths

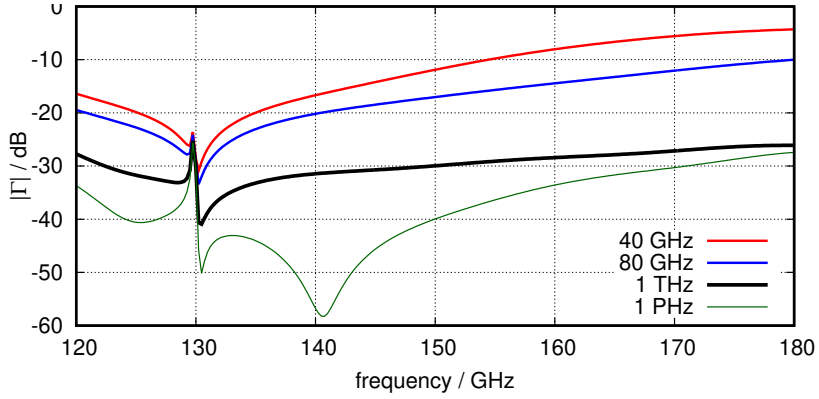

Fig. 3.9.: Reflections of the zero-order matched $\tilde{g}(t)$ for different filter bandwidths, without their non-causal parts

3.6.1. Improved wavenumber

The broadband matched boundary condition tested in the examples in chapter 3.5 involves a zero-order polynomial for a matched boundary. This means that

$$a_0 = s \quad \text{and} \quad a_1 = 0 \quad \text{in (3.35)}$$

For the boundary on the left-hand side $s = 1$ and for the right-hand side $s = -1$. According to (2.31), in order to improve the matched boundary condition by improving the approximation of the axial wave number, it should be

$$a_0 = s \quad \text{and} \quad a_1 = -\frac{s}{2\,(\omega_0 + \omega_c)}$$

After applying this in (3.35), the simulation shows a better matched boundary. It can be seen in fig. 3.10, that the reflection coefficient is improved over 15 dB with the polynomial compensation of $k_{\|}$. The reflection still can not reach the theoretical value, for the reason of the numerical inaccuracy. However for practical applications, the behaviour of this new broadband boundary condition is completely appropriate.

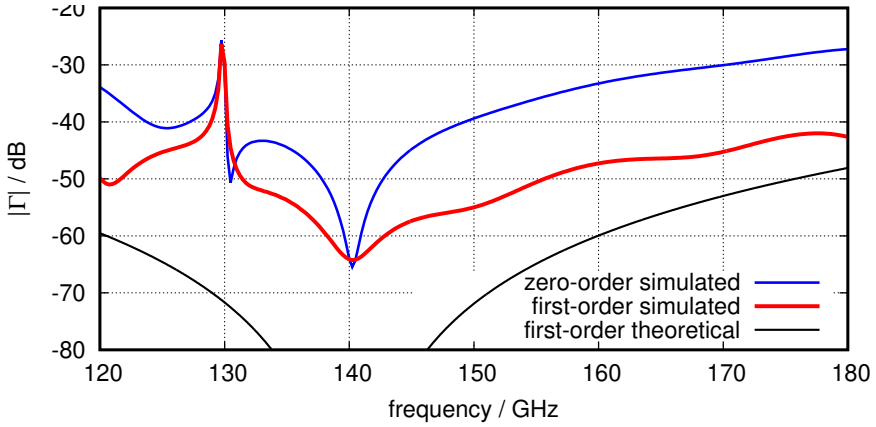

Fig. 3.10.: Reflection coefficient of the matched boundary with a first-order polynomial improving the approximation of the axial wavenumber

3.6.2. User defined reflection

Though a PML (Perfect Matching Layer) approach may produce less reflection [15] than the result in fig. 3.10, one highlight of the developed boundary condition formulation is the introduction of a frequency-dependent reflection coefficient, of which the PML is not capable.

A first-order polynomial in the boundary condition (3.35) corresponds to a line in the two dimensional space (Z, ω). This line has two free variables a_0 and a_1. A user-defined reflection coefficient can be determined by two arbitrary points on the line. From

$$Z = \frac{1+\Gamma}{1-\Gamma} = a_0 + a_1\omega$$

there is

$$\Gamma = \frac{Z-1}{Z+1} = \frac{a_1\omega + a_0 - 1}{a_1\omega + a_0 + 1} \tag{3.36}$$

A user-defined curve of reflection coefficient will be demonstrated as a concrete example. The curve passes through two points:

- Instead of the carrier frequency of 140 GHz, let the boundary have perfect matching at 150 GHz
- The reflection at 140 GHz is assigned to be $0.05 + 0j$, which is -26 dB.

frequency	relative ω	Γ	Z
140 GHz	0	0.05	1.10526
150 GHz	20π GHz	0	1

Table 3.4.: Parameters of a user-defined curve of reflection coefficient ($Z = a_1\omega + a_0$)

Calculated from table 3.4, the coefficients of the polynomial are

$$a_0 = 1.105263\,s \quad \text{and} \quad a_1 = -1.675316 \times 10^{-12}\,s$$

where $s = 1$ for the left-hand side boundary, $s = -1$ for the right-hand side.

Although the simulation only includes a first-order polynomial, the improvement in $k_\parallel$ can still be incorporated. The series for the user-defined Z and for the improved $k_\parallel$ (section 2.1.3) can be merged in the way, that both polynomials are firstly multiplied and then the higher-order terms of their product are omitted.

$$(a_1'\omega + a_0')\,(a_1''\omega + a_0'') = \cancel{a_1' a_1'' \omega^2} + \underbrace{(a_1' a_0'' + a_0' a_1'')}_{=:a_1}\,\omega + \underbrace{a_0' a_0''}_{=:a_0}$$

Thus, the polynomial coefficients of this user-defined reflection coefficient with an improved $k_\parallel$ are

$$a_0 = 1.105263\,s \quad \text{and} \quad a_1 = -\left(\frac{1.105263}{2(\omega_0 + \omega_c)} + 1.675316 \times 10^{-12}\right) s$$

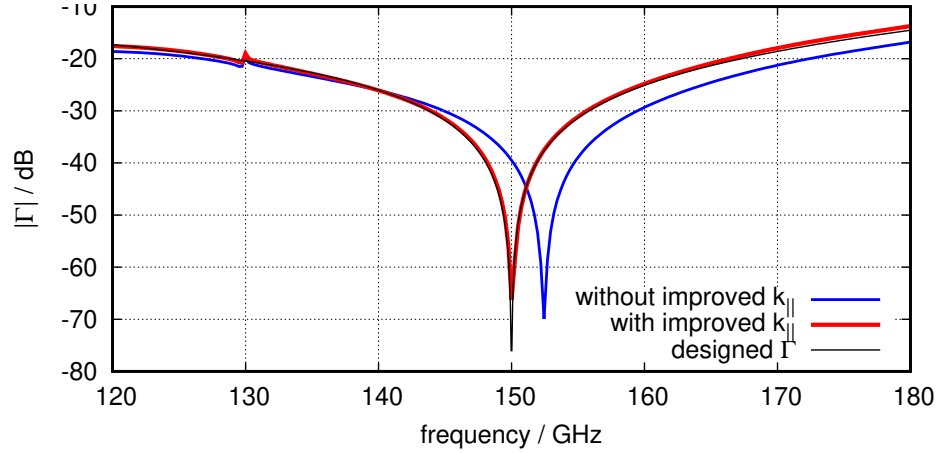

Fig. 3.11.: Simulated results of a user-defined reflection coefficient, compared with the theoretical one

Results of both concepts are plotted in fig. 3.11. In the later concept with an improved $k_{\parallel}$, the simulated result concurs fully with the theoretical one: it has an almost perfect matching at 150 GHz and −26 dB at 140 GHz, exactly the same as the designed values.

Although only a first-order polynomial is used, the resulting user-defined reflection coefficient can be physically very relevant. This is apparent from the fig. 3.12, showing the reflection coefficient at the gyrotron window.

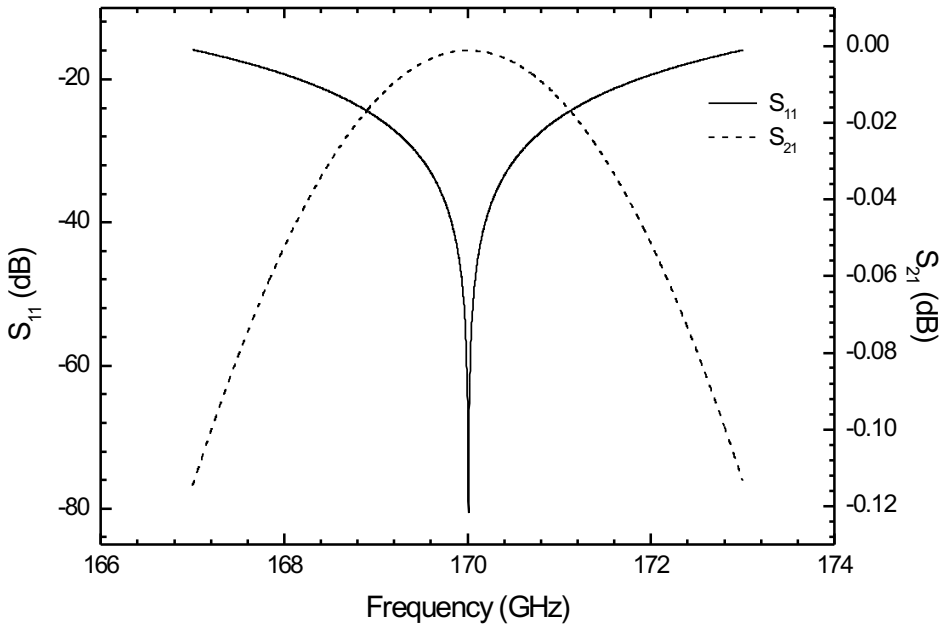

Fig. 3.12.: Reflection and transmission as a function of frequency for a single disc diamond window [1]

3.7. Summary

In this chapter, the numerical details of the test program are explained. Two approaches for calculating the inverse Fourier transform and the convolution are tested.

If the Fourier transform and convolution are performed in the space of Lebesgue integrable functions through a exponential filter, the signal in time domain is non-causal. In case of taking the values in the future into account by delaying the boundary condition, the numerical equation becomes explicit, which causes instabilities. However, this approach can work if the future is neglected, but only for the low-order polynomials.

Performing the Fourier transform and convolution in the space of tempered distributions requires the numerical time derivative of $\frac{\partial A}{\partial f}$. This is not accurate enough at high orders. However when only the first order is used, the scheme works very well.

It has been tested, that the new formulation proposed in the thesis improves the existing broadband boundary condition by 15 dB and can exactly reproduce a user-defined complex reflection coefficient in the first-order (see fig. 3.10 and 3.11). These two points advance further the state of the art.

4. Summary and outlook

Investigation of gyrotron operating regimes with dynamic after cavity interaction [6, 7] or side-bands in the spectrum [8], requires a broadband boundary condition for the RF-field in the simulation of the gyrotron cavity. Furthermore, in order to simulate the realistic reflections from the gyrotron components before and after the cavity, the boundary condition should be able to account for a frequency-dependent reflection. All the above motivated the study on advanced formulation and implementation of the boundary condition.

Starting from the idea of existing broadband boundary conditions [14, 16], an improved formulation based on the inverse Fourier transform is proposed in this master thesis, in the way, that several physical variables are represented by polynomial series. The new formulation achieves not only a quantitative improvement of the existing matched broadband boundary condition, but also allows the user to define a frequency dependent curve of complex reflection coefficients, which is on the way to provide the possibility for emulating the profile of the reflection in reality.

The main task in this new formulation is performing an inverse Fourier transform on a polynomial-like function and then convoluting it with a discrete signal. Two solutions are investigated. In the first solution, the function to be transformed is filtered into the space of Lebesgue integrable functions by a compensated exponential filter. Afterwards the inverse Fourier is done by the integral formula, which can be found in the most text books for electrical engineering. This filter has to be non-causal in order to keep the original phase unchanged. The other solution treats the polynomial-like function with the convolution as a linear functional and the inverse Fourier transform is performed in the space of tempered distributions. Due to the properties of distributions, the polynomial is transferred into the time derivatives of the other component in the convolution — the time discrete signal.

A program was written during the master thesis to test different boundary conditions. The code for each boundary condition was so modularized, that its object files can be directly linked with EURIDICE. Both approaches have been numerically implemented and verified, in the case of a matched boundary (zero reflection) for the zero-order polynomial. Then a first-order polynomial was investigated in the frame of the formulation as a tempered distribution, which appeared to be more stable than the Lebesgue inte-

grable function. The numerical result shows, that this first-order polynomial improves the existing matched boundary condition by about 15 dB (see fig. 3.10) and can exactly reproduce a user-defined reflection in the first-order (fig. 3.11). These two aspects are beyond the current state-of-the-art of boundary conditions in fast gyrotron simulations.

The improvement of the broadband boundary condition with a first-order polynomial can be seen in two ways:

1. For a given time-step, the quality of broadband matching in the boundary condition is enhanced.

2. For a given quality of matching, a larger time-step can be used and this speeds-up the calculation significantly.

Furthermore, the possibility to introduce a user-defined, frequency-dependent $\Gamma(\omega)$ opens the way towards modelling of realistic reflections inside and outside of the gyrotron.

The present thesis strongly motivates further investigations on several subjects. First, the developed boundary condition should be coupled to EURIDICE, in order to enable advanced modelling of realistic gyrotrons. Because the equations derived in this thesis and used in the test program are compatible with EURIDICE, a port (from C++ to Fortran for EURIDICE) of the boundary condition is also conceivable. Regarding the investigated formulation of the boundary condition, other methods may be tried to circumvent the instability caused by the non-causal filter. As mentioned before, it has been observed, that there is a possibility to compensate some non-causality with a constant or impulse function. Moreover, there could also be another way to do the high-order time derivative on the envelope function more accurately. Finally, the boundary condition developed in this thesis already supports a user-defined reflection at the first order in the (Z, ω) plane, but it was not investigated, how the reflection will be. It has to be analysed or measured, how good it is to approximate the reflection using the first order polynomial for the equivalent wave-impedance.

In the end, it should be emphasised, that the developed concept of the broadband boundary condition is a general approach for all of cavities as well as waveguides and is not limited only in the gyrotron simulation.

Appendix A.

Fourier transforms

Fourier for the $\mathcal{L}^1$-space

A function $f : \mathbb{R} \to \mathbb{R}$ belongs to the $\mathcal{L}^1(\mathbb{R})$ space, if it is Lebesgue integrable

$$\int_{-\infty}^{+\infty} |f(x)| \, \mathrm{d}x < \infty \tag{A.1}$$

This condition can be extended into $\mathbb{R} \to \mathbb{C}$ by considering the real and imaginary parts separately. Instead of $\int_{-\infty}^{+\infty}$, any integral over the whole real axis will be written just as $\int$ for simplicity. The Fourier and inverse Fourier transform for function in the $\mathcal{L}^1$-space are defined as

$$(\mathcal{F} f)(\omega) := \frac{1}{\sqrt{2\pi}} \int f(t) \, e^{-j\omega t} \, \mathrm{d}t \tag{A.2a}$$

$$(\mathcal{F}^{-1} \hat{f} \,)(t) := \frac{1}{\sqrt{2\pi}} \int \hat{f}(\omega) \, e^{j\omega t} \, \mathrm{d}\omega \tag{A.2b}$$

where $\mathcal{F}^{\pm 1}$ maps a function from $\mathcal{L}^1$-space into $\mathcal{L}^\infty$-space.

Fourier for the $\mathcal{S}$-space

A function $\varphi \in \mathcal{C}^\infty(\mathbb{R})$ belongs to the (one dimensional) Schwartz space $\mathcal{S}(\mathbb{R})$, if for any arbitrary index $p, q \in \mathbb{N}$

$$\left\| x^p \left(\frac{\mathrm{d}}{\mathrm{d}x} \right)^q \varphi(x) \right\|_\infty = \sup_{x \in \mathbb{R}} \left| x^p \left(\frac{\mathrm{d}}{\mathrm{d}x} \right)^q \varphi(x) \right| < \infty \tag{A.3}$$

The Schwartz space is also called space of rapidly decreasing functions. Functions in this space decrease quicker than any polynomials at $x \to \infty$. $\mathcal{S}$ is dense in $\mathcal{L}^2$ and $\mathcal{S}(\mathbb{R})$ belongs to $\mathcal{L}^1(\mathbb{R})$. This is because, if $\varphi \in \mathcal{S}(\mathbb{R})$, then by the definition of $\mathcal{S}$

$$\left| (1 + x^2) \, \varphi(x) \right| \leq |C| \quad \text{, } C \text{ is a constant and } x \in \mathbb{R}$$

and

$$|\varphi(x)| \leq \frac{|C|}{1+x^2}$$

Then

$$\int |\varphi(x)| \, \mathrm{d}x \leq \int \frac{|C|}{1+x^2} \, \mathrm{d}x = |C| \left[\arctan x\right]_{-\infty}^{+\infty} = \pi \, |C| < \infty$$

Therefore φ belongs to $\mathcal{L}^1(\mathbb{R})$. As a result, the Fourier transform defined in (A.2) can be used directly. Furthermore, the $\mathcal{F} : \mathcal{S} \to \mathcal{S}$ is bijective [17].

Fourier for the $\mathcal{S}'$-space

$\mathcal{S}'$ space is the space of tempered distributions. Distributions or generalized functions are continuous linear functionals. In this thesis, a local integrable function $f(x)$ and its induced functional $f(\varphi)$ will be treated as the same thing:

$$f(\varphi) = \langle f, \varphi \rangle := \int f(x) \, \varphi(x) \, \mathrm{d}x \tag{A.4}$$

A **tempered distribution** is a distribution, which is defined on the $\mathcal{S}$ space. If $f(x)$ is a tempered distribution, then exists the integral

$$\langle f, \varphi \rangle = \int f(x) \, \varphi(x) \, \mathrm{d}x \quad \text{for } \varphi \in \mathcal{S}$$

which induces a continuous linear functional. Two distributions f, g are equal, if

$$\langle f, \varphi \rangle = \langle g, \varphi \rangle \quad \text{for every } \varphi$$

Except the linearity, distributions possess a useful property for the partial derivative

$$\left\langle \frac{\partial}{\partial x} f \, , \, \varphi \right\rangle = - \left\langle f \, , \, \frac{\partial}{\partial x} \varphi \right\rangle \tag{A.5}$$

The Fourier and inverse Fourier transform $\mathcal{F} f$ for $f \in \mathcal{S}'$ is defined as [17]

$$\langle \mathcal{F} f, \, \varphi \rangle = \langle f, \, \mathcal{F} \varphi \rangle \tag{A.6a}$$

$$\langle \mathcal{F}^{-1} f, \, \varphi \rangle = \langle f, \, \mathcal{F}^{-1} \varphi \rangle \tag{A.6b}$$

An example is $\mathcal{F}\delta = \frac{1}{\sqrt{2\pi}}$ because

$$\langle \mathcal{F}\delta, \varphi \rangle = \langle \delta, \mathcal{F}\varphi \rangle = \frac{1}{\sqrt{2\pi}} \int \varphi(t) \, e^{-j\omega t} \, \mathrm{d}t \bigg|_{\omega=0} = \left\langle \frac{1}{\sqrt{2\pi}} \, , \, \varphi \right\rangle$$

For the Fourier in $\mathcal{S}'$, the following relation is still valid (for proof see [17]).

$$\mathcal{F} \left\{ \left(\frac{\partial}{\partial t} \right)^n f \right\} = (j\omega)^n \, \mathcal{F} f \tag{A.7}$$

Lemmas

Lemma 1.

$$f(\omega) * \delta(\omega + \Delta\omega) = f(\omega + \Delta\omega)$$

Proof.

$$f(\omega) * \delta(\omega + \Delta\omega) = \int f(\omega - x)\ \delta(x + \Delta\omega)\ \mathrm{d}x\ .$$

Let $y := x + \Delta\omega$ then

$$\begin{aligned} f(\omega) * \delta(\omega + \Delta\omega) &= \int f(\omega - y + \Delta\omega)\ \delta(y)\ \mathrm{d}y \\ &= f(\omega + \Delta\omega)\ . \end{aligned}$$

□

Lemma 2. *If the Fourier transform for $\mathcal{L}^1$ is defined as*

$$\mathcal{F}^{\pm 1}\varphi = \frac{1}{\sqrt{2\pi}} \int \varphi(x)\ e^{\mp j\,\xi\,x}\ \mathrm{d}x$$

then

$$\mathcal{F}^{\pm 1}(\varphi * \psi) = \sqrt{2\pi}\ \left(\mathcal{F}^{\pm 1}\varphi\right) \cdot \left(\mathcal{F}^{\pm 1}\psi\right) \tag{A.8a}$$

$$\mathcal{F}^{\pm 1}(\varphi \cdot \psi) = \frac{1}{\sqrt{2\pi}}\ \left(\mathcal{F}^{\pm 1}\varphi\right) * \left(\mathcal{F}^{\pm 1}\psi\right) \tag{A.8b}$$

Proof. Firstly (A.8a) will be proven. According to the definitions there is

$$\begin{aligned} \mathcal{F}^{\pm 1}\Big\{\varphi(\xi) * \psi(\xi)\Big\} &= \frac{1}{\sqrt{2\pi}} \int \left[\int \varphi(\xi - u)\,\psi(u)\,\mathrm{d}u\ \ e^{\mp j\,\xi\,x}\right] \mathrm{d}\xi \\ &= \frac{1}{\sqrt{2\pi}} \iint \varphi(\xi - u)\,\psi(u)\,e^{\mp j\,\xi\,x}\ \mathrm{d}u\ \mathrm{d}\xi\ , \end{aligned}$$

and using the Fubini's theorem yields

$$\mathcal{F}^{\pm 1}\Big\{\varphi(\xi) * \psi(\xi)\Big\} = \frac{1}{\sqrt{2\pi}} \iint \varphi(\xi - u)\,\psi(u)\,e^{\mp j\,\xi\,x}\ \mathrm{d}\xi\ \mathrm{d}u\ .$$

Since $\psi(u)$ is independent of ξ

$$\mathcal{F}^{\pm 1}\Big\{\varphi(\xi) * \psi(\xi)\Big\} = \frac{1}{\sqrt{2\pi}} \iint \varphi(\xi - u)\,e^{\mp j\,\xi\,x}\ \mathrm{d}\xi\ \psi(u)\ \mathrm{d}u\ .$$

Defining $v = \xi - u$, since the integral is on the entire $\mathbb{R}$ axis, omitting the shifting u does not affect the result

$$\begin{aligned}
&\mathcal{F}^{\pm 1}\Big\{\varphi(\xi) * \psi(\xi)\Big\} = \frac{1}{\sqrt{2\pi}} \iint \varphi(v)\, e^{\mp j\, v\, x} e^{\mp j\, u\, x}\, \mathrm{d}(\cancel{v+u})\, \psi(u)\, \mathrm{d}u \\
=&\frac{1}{\sqrt{2\pi}} \iint \varphi(v)\, e^{\mp j\, v\, x}\, \mathrm{d}v\, e^{\mp j\, u\, x}\, \psi(u)\, \mathrm{d}u \\
=&\frac{1}{\sqrt{2\pi}} \int \varphi(v)\, e^{\mp j\, v\, x}\, \mathrm{d}v \int \psi(u)\, e^{\mp j\, u\, x}\, \mathrm{d}u \\
=&\sqrt{2\pi}\ (\mathcal{F}^{\pm 1}\varphi) \cdot (\mathcal{F}^{\pm 1}\psi)\ .
\end{aligned}$$

So is (A.8a) proved. Denoting

$$\begin{aligned}
f :=& \mathcal{F}^{\pm 1}\varphi\ , \\
g :=& \mathcal{F}^{\pm 1}\psi\ ,
\end{aligned}$$

then (A.8b) can be derived from (A.8a):

$$\begin{aligned}
\mathcal{F}^{\pm 1}\Big(\mathcal{F}^{\mp 1} f\ *\ \mathcal{F}^{\mp 1} g\Big) =& \sqrt{2\pi}\ f \cdot g \\
\mathcal{F}^{\mp 1} f\ *\ \mathcal{F}^{\mp 1} g =& \sqrt{2\pi}\ \mathcal{F}^{\mp 1}\left(f \cdot g\right)\ .
\end{aligned}$$

□

Lemma 3.

$$\mathcal{F}^{-1}\Big\{\delta(\omega + \Delta\omega)\Big\} = \frac{1}{\sqrt{2\pi}}\, e^{-j\,\Delta\omega\, t}$$

Proof. $\forall \varphi \in \mathcal{S}$

$$\begin{aligned}
&\mathcal{F}^{-1}\Big\{\delta(\omega + \Delta\omega)\Big\} \\
=&\Big\langle \mathcal{F}^{-1}\Big\{\delta(\omega + \Delta\omega)\Big\}\ ,\ \varphi \Big\rangle := \langle \delta(\omega + \Delta\omega)\ ,\ \mathcal{F}^{-1}\varphi \rangle \\
=&\frac{1}{\sqrt{2\pi}} \int \delta(\omega + \Delta\omega) \left[\int \varphi\, e^{j\omega t}\, \mathrm{d}t\right] \mathrm{d}\omega \quad \text{, let } \Omega = \omega + \Delta\omega \\
=&\frac{1}{\sqrt{2\pi}} \int \varphi\, e^{j(\Omega - \Delta\omega)t}\, \mathrm{d}t \Big|_{\Omega=0} = \frac{1}{\sqrt{2\pi}} \left\langle e^{-j\,\Delta\omega\, t}\ ,\ \varphi \right\rangle \\
=&\left\langle \frac{1}{\sqrt{2\pi}}\, e^{-j\,\Delta\omega\, t}\ ,\ \varphi \right\rangle \\
=&\frac{1}{\sqrt{2\pi}}\, e^{-j\,\Delta\omega\, t}
\end{aligned}$$

□

Bibliography

[1] Kartikeyan, M. V. ; Borie, Edith ; Thumm, Manfred K. A.: Gyrotrons : high power microwave and millimeter wave technology. Berlin : Springer, 2004 (Advanced texts in physics). – ISBN 3–540–40200–4

[2] Kern, S.: Numerische Simulation der Gyrotron-Wechselwirkung in koaxialen Resonatoren, Karlsruhe Institute of Technology, Diss., 2006. – FZKA 5837

[3] Avramides, K. A. ; Pagonakis, I. G. ; Iatrou, C. T. ; Vomvoridis, J. L.: EURIDICE: A code-package for gyrotron interaction simulations and cavity design. In: European Physical Journal Web of Conferences Bd. 32, 2012 (European Physical Journal Web of Conferences), S. 4016

[4] Dumbrajs, O.: COAXIAL. 2001. – Helsinki University of Technology

[5] Alberti, S. ; Tran, T M. ; Avramides, K. A. ; Li, F. ; Hogge, J.-P.: Gyrotron parasitic-effects studies using the time dependent self-consistent monomode code TWANG. October 2011. – 36th Int. Conf. Infrared Millimeter THz Waves, Houston ,TX, USA, Conference proceedings Tu5.15

[6] Kern, S. ; Avramides, K.A. ; Choudhury, A.R. ; Dumbrajs, O. ; Gantenbein, G. ; Illy, S. ; Samartsev, A. ; Schlaich, A. ; Thumm, M.: Simulation and experimental investigations on dynamic after cavity interaction (ACI). In: Infrared Millimeter and Terahertz Waves (IRMMW-THz), 2010 35th International Conference on, 2010, S. 1–2

[7] Schlaich, A. ; Choudhury, A.R. ; Gantenbein, G. ; Illy, S. ; Kern, S. ; Lievin, C. ; Samartsev, A. ; Thumm, M.: Examination of parasitic after-cavity oscillations in the W7-X series gyrotron SN4R. In: Infrared, Millimeter and Terahertz Waves (IRMMW-THz), 2011 36th International Conference on, 2011. – ISSN 2162–2027, S. 1–2

[8] Alberti, S. ; Ansermet, J.-Ph. ; Avramides, K. A.: Experimental study from linear to chaotic regimes on a terahertz-frequency gyrotron oscillator. In: Physics of Plasmas 19 (2012)

[9] Dammertz, G. ; Alberti, S. ; Bariou, D. ; Brand, P. ; Braune, H. ; Erckmann, V. ; Gantenbein, G. ; Giguet, E. ; Heidinger, R. ; Hogge, J.P. ; Kasparek, W. ; Laqua, H.P. ; Liévin, C. ; Leonhardt, W. ; Michel, G. ; Müller, G. ; Neffe, G. ; Piosczyk, B. ; Schmid, M. ; Thumm, M.: 140GHz high-power gyrotron development for the stellarator W7-X. In: Fusion Engineering and Design 74 (2005). – ISSN 0920–3796

[10] Avramides, K. A. ; Ioannidis, Z. C. ; Tigelis, I. G. ; Chelis, I. G. ; Vomvoridis, J. L. ; M., Tran T.: Numerical tool development for gyrotron design and simulation. 2013. – EFDA-PPPT Task Agreement WP12-DAS-HCD-EC-04-01, Final Report

[11] Hoffmann, K.A. ; Chiang, S.T.: Computational Fluid Dynamics. Engineering Education System, 2000 (Computational Fluid Dynamics). – ISBN 9780962373107

[12] Quarteroni, Alfio ; Saleri, Fausto: Wissenschaftliches Rechnen mit MATLAB. Berlin : Springer, 2006 (Springer-Lehrbuch). – ISBN 3–540–25005–0; 978–3–540–25005–0

[13] Avramides, K.A. u. a.: Improvements of beam-wave interaction modelling in Euridice. Sep 2012. – in Design and Development of the European Gyrotron, F4E-2009GRT-049-01, Final Report, task 2.3, Annex 7

[14] Tran, Trach-Minh ; Brunner, Stephan ; Alberti, Stefano: Non-Reflecting Boundary Conditions for the Time-Dependent Wave envelope Equation in a Cylindrical Cavity. Februar 2012. – F4E-EGYC Grant Agreement: Design and Development of the European Gyrotron ("CCGDS7"), Contract Ref. No.: F4E-2009-GRT-049-01, Final Report, Task 2.3, Annex 9

[15] Taflove, Allen ; Hagness, Susan C.: Computational electrodynamics : the finite-difference time-domain method. 3. ed. Artech House, 2005 (Artech House antennas and propagation library). – ISBN 1–58053–832–0; 978–1–58053–832–9

[16] Avramides, K. A. ; Ioannidis, Z. C. ; Tigelis, I. G. ; Chelis, I. G. ; Vomvoridis, J. L. ; M., Tran T.: Report for Task Agreement WP12-DAS-HCD-EC-04-01. 12 2012

[17] Walter, W.: Einführung in die Theorie der Distributionen. B.I.-Wissenschaftsverlag, Bibliographisches Institut & F.A. Brockhaus, 1994. – ISBN 9783411170234

Karlsruher Institut für Technologie

Institut für Hochfrequenztechnik und Elektronik

Chuanren Wu

Master thesis: **Investigations on Improving Broadband Boundary Conditions in Gyrotron Interaction Modelling**

Zeitraum: **05.08.2013 – 05.02.2014**

Betreuer: **Dr. Stefan Illy ; Dr. Konstantinos A. Avramidis**

Gyrotrons are microwave tubes capable of providing mega-watt power at millimetric wavelengths. The microwave power is produced by the conversion of the kinetic energy of an electron beam to electromagnetic wave energy. Simulations of the beam-wave interaction in the gyrotron cavity are essential for gyrotron design, as well as theoretical and experimental studies.

In the usual gyrotron operation the spectrum of the generated radiation is concentrated around the nominal frequency. For this reason, the usual simulations consider only a narrow-band output spectrum (e.g. several GHz bandwidth comparing with the working frequency in the range of 100-200 GHz). As a result, the typical existing codes use a single-frequency radiation boundary condition for the generated electromagnetic field in the cavity. This condition is matched only at one frequency. However, there are two important aspects, which motivate an advanced formulation and implementation of the cavity boundary condition. Firstly, the occurrence of broadband effects (which may be several tens of GHz) in some cases , like dynamic after-cavity-interaction or modulation side-bands, requires a broadband boundary condition. Secondly, there are reflections from inside and outside of the gyrotron, which can only be considered in the simulation through a boundary condition with user-defined, frequency-dependent reflections.

This master thesis proposes an improved formulation of the broadband boundary condition in the self-consistent, beam-wave interaction code EURIDICE. In this new formulation, two physical variables — the wave impedance and the axial wavenumber are expanded in polynomial series in the frequency domain. Because the beam-wave interaction process is simulated transiently in the time domain, the boundary condition should be also expressed in the time domain. This involves a non-trivial inverse Fourier transform, for which two solutions are proposed, tested and validated.

It has been shown that, through the newly developed formulation, the existing matched boundary condition (that should yield zero-reflection in ideal case) can be improved by 15 dB even with a first-order polynomial series. Moreover, a user-defined, frequency-dependent complex reflection coefficient can be introduced. This was not possible with the previously existing boundary condition in EURIDICE.

Postanschrift: Institut für Hochfrequenztechnik und Elektronik
Kaiserstraße 12
D-76131 Karlsruhe

Gebäude: Engesserstraße 5, Geb. 30.10

Tel.: +49 (0) 721 608 4 2522
Sekr.: +49 (0) 721 608 4 2523
Fax: +49 (0) 721 608 4 5027
E-Mail: info@ihe.kit.edu
Web: www.ihe.kit.edu